Aerospace Science and Technology 154 (2024) 109478

Contents lists available at ScienceDirect

Aerospace Science and Technology

journal homepage: www.elsevier.com/locate/aescte

On the dynamics of improved perovskite solar cells: Introducing SVM-DNN-GA algorithm to predict dynamical information

Qian Zhang [a], Qinghe Xu [b,*], Mohammed A. El-Meligy [c,d], Mehdi Tlija [e]

[a] School of Data Science and Artificial Intelligence, Wenzhou University of Technology, Wenzhou, Zhejiang 325035, China
[b] School of Information and Technology, Wenzhou Business College, Wenzhou, Zhejiang 325006, China
[c] Jadara University Research Center, Jadara University, Jordan
[d] Applied Science Research Center, Applied Science Private University, Amman, Jordan
[e] Department of Industrial Engineering, College of Engineering, King Saud University, P.O. Box 800 Riyadh 11421, Saudi Arabia.

A R T I C L E I N F O

Keywords:
Improved perovskite solar cell
FG-TPMS
Trigonometric functions
Elastic substrate
SVM-DNN-GA algorithm

A B S T R A C T

This study presents an innovative approach to enhancing the performance of perovskite solar cells through the integration of a functionally graded triply periodic minimal surface (FG-TPMS) layer. The research focuses on the mechanical and vibrational characteristics of doubly curved panels embedded with three distinct iterations of the FG-TPMS model: the primitive, gyroid, and wrapped package graph (IWP). By employing higher-order shear deformation theory (HSDT), the analysis accounts for the complex geometrical and material gradations within the FG-TPMS structures. An advanced analytical method utilizing trigonometric functions is developed to accurately predict the natural frequencies and mode shapes of these novel composite structures. In order to assess the vibrations of TPMS-reinforced perovskite solar cells surrounded by an elastic foundation, this work proposes the implementation of a novel Support Vector Machine (SVM)-deep neural network (DNN)-Genetic Algorithm (GA) employing mathematical modeling datasets. Using the SVM-DNN-GA algorithm, predicted accuracy is improved. In order to simulate and forecast the vibrational behavior of the reinforced solar cells, the integrated methodology makes use of the advantages of each technique. The results indicate that the integration of FG-TPMS layers significantly enhances the mechanical stability of the perovskite solar cells. The application of HSDT reveals detailed insights into the dynamic responses of the doubly curved panels, highlighting the potential for fine-tuning their vibrational characteristics to further improve solar cell performance. This research underscores the potential of FG-TPMS structures in advancing solar cell technology, providing a foundation for future studies to explore the integration of complex geometries and material gradations in photovoltaic applications.

1. Introduction

Functionally graded triply periodic minimal surfaces (FG-TPMS) play a crucial role in engineering applications due to their unique structural and material properties [1]. These structures combine the benefits of functionally graded materials (FGMs) with the inherent advantages of minimal surface geometries, resulting in optimized performance across various applications [2]. FG-TPMS structures exhibit superior mechanical properties such as high strength-to-weight ratios, making them ideal for lightweight yet robust components in aerospace and automotive industries [3]. The complex geometry of FG-TPMS ensures optimal stress distribution, reducing the likelihood of material failure under load and enhancing the durability of engineering components [4]. Their intricate structures are excellent for energy absorption, making them suitable for impact-resistant applications, including protective gear and crash-worthy structures. FG-TPMS materials can be designed to have tailored thermal conductivity, providing efficient heat dissipation in electronics and heat exchangers [5]. They also offer excellent acoustic properties, useful in noise reduction applications. The ability to customize the material gradation within FG-TPMS allows for targeted performance enhancements, catering to specific engineering needs. In biomedical engineering, FG-TPMS structures are used to create implants and prosthetics that mimic the mechanical properties of natural bone [6]. The interconnected porosity of these structures supports cell growth and nutrient transport, promoting better integration with biological tissues. In civil engineering, FG-TPMS can be

* Corresponding author.
E-mail address: 247312662@qq.com (Q. Xu).

https://doi.org/10.1016/j.ast.2024.109478
Received 6 July 2024; Received in revised form 4 August 2024; Accepted 8 August 2024
Available online 10 August 2024

used to design lightweight, strong, and durable construction materials. The high surface area-to-volume ratio of FG-TPMS is beneficial for catalysis and filtration applications [7]. Additive manufacturing techniques facilitate the production of complex FG-TPMS structures, allowing for precise control over their geometry and material composition [8]. This capability opens up new possibilities for innovative design and material optimization in various engineering fields [9]. Finally, the versatility and adaptability of FG-TPMS structures make them a promising solution for addressing the ever-evolving challenges in modern engineering [10].

Perovskite solar cells are revolutionizing the field of renewable energy with their remarkable properties and engineering applications [11]. These solar cells offer high power conversion efficiencies, rivaling traditional silicon-based cells while being significantly cheaper to produce [12]. Their low cost is due to the use of abundant and inexpensive raw materials and relatively simple manufacturing processes, making them economically viable for widespread use [13]. Perovskite solar cells exhibit a high absorption coefficient, allowing them to absorb a broad spectrum of sunlight efficiently, which is critical for maximizing energy conversion [14]. They are also versatile, capable of being fabricated on flexible substrates, opening up new possibilities for integration into various surfaces and portable electronic devices [15]. Their lightweight nature further enhances their applicability in areas where weight is a critical factor, such as in aerospace and engineering industries [16]. These solar cells can be manufactured using solution-based processes, which are less energy-intensive compared to the high-temperature methods required for silicon cells, contributing to their lower environmental impact [17]. The tunable bandgap of perovskite materials allows for the optimization of light absorption and energy conversion, making them suitable for tandem solar cells that combine different materials to achieve even higher efficiencies [18]. Perovskite solar cells have shown excellent performance under low-light conditions, making them ideal for indoor and diffuse light applications [19]. Their rapid advancements in stability and durability are addressing initial concerns, paving the way for their use in long-term applications. These cells can also be integrated with existing silicon solar cells to create hybrid systems that boost overall efficiency and reduce costs [19]. The scalability of perovskite solar cell production is another key advantage, enabling large-scale deployment for utility-scale power generation. Their potential for building-integrated photovoltaics (BIPV) allows for the creation of energy-harvesting windows and facades, contributing to sustainable urban development [20]. The ability to produce semi-transparent perovskite solar cells expands their use in aesthetic applications without compromising on energy generation [21].

Modeling plays a pivotal role in engineering applications, providing a fundamental framework for understanding, predicting, and optimizing complex systems and processes [22,23]. It allows engineers to create virtual representations of physical phenomena, enabling the analysis of behavior under various conditions without the need for costly and time-consuming experiments [24]. Accurate modeling helps in designing systems and components with optimal performance, ensuring they meet specified requirements and constraints [25]. It facilitates the exploration of design alternatives and the assessment of their impacts, leading to more informed decision-making [26]. Through simulation, modeling can predict potential failures and identify weaknesses, enhancing the reliability and safety of engineering solutions [27]. In the development of new materials, modeling helps predict properties and behavior, accelerating innovation and reducing the need for extensive experimental testing [28]. It also plays a crucial role in understanding and mitigating environmental impacts, allowing engineers to design sustainable and eco-friendly solutions [29]. In manufacturing, modeling optimizes processes, improves efficiency, and reduces waste by simulating production lines and identifying bottlenecks [30]. It supports the integration of new technologies, such as additive manufacturing, by providing insights into process parameters and material behavior [31]. For infrastructure projects, modeling assists in planning, design, and maintenance, ensuring the longevity and safety of structures like bridges, roads, and buildings [32]. It is essential in aerospace and automotive industries for simulating aerodynamics, structural integrity, and system performance, leading to the development of high-performance vehicles and aircraft [33]. Modeling is integral to the advancement of renewable energy technologies, such as wind and solar power, by optimizing system design and predicting energy output [34]. It aids in the development of smart grids, enhancing the efficiency and reliability of power distribution networks [35].

This work introduces a novel method for improving perovskite solar cells' efficiency by using an FG-TPMS layer. The study focuses on the mechanical and vibrational properties of doubly curved panels embedded with the primitive, gyroid, and IWP iterations of the FG-TPMS model. The research takes into consideration the intricate geometrical and material gradations present in the FG-TPMS structures by using HSDT. The panels' behavior under operating circumstances is realistically simulated since they are based on an elastic substrate. The inherent frequencies and mode forms of these innovative composite structures are reliably predicted by means of an advanced mathematical technique based on trigonometric functions. The findings show that the mechanical stability of the perovskite solar cells are greatly improved by the incorporation of FG-TPMS layers. Every iteration of the FG-TPMS exhibits distinct benefits: the IWP design guarantees optimum material efficiency, the gyroid model gives optimal stress distribution, and the primitive structure offers better isotropic mechanical characteristics. Through the use of HSDT comprehensive insights into the doubly curved panels' dynamic responses are revealed, underscoring the possibility of further enhancing solar cell efficiency by fine-tuning their vibrational features. In order to assess the vibrations of TPMS-reinforced perovskite solar cells surrounded by an elastic foundation, this work proposes the implementation of a novel SVM-DNN-GA employing mathematical modeling datasets. Using the SVM-DNN-GA algorithm, predicted accuracy is improved. In order to simulate and forecast the vibrational behavior of the reinforced solar cells, the integrated methodology makes use of the advantages of each technique. The potential of FG-TPMS structures to advance solar cell technology is highlighted by this study, laying the groundwork for further investigations into the integration of intricate geometries and material gradations in photovoltaic applications.

2. Mathematical modeling

We present perovskite solar cells in Fig. 1. As can be seen, a solar cell is made up of six layers, with glass at the outermost and the FG-TPMS layer at the innermost. Fig. 1 displays the whole geometry of this structure together with a three-dimensional schematic depiction.

In addition to providing a thorough explanation of additional geometrical requirements, the results section presents the material properties of each layer in detail.

2.1. Mechanical properties of FG-TPMS materials

This paper examines the wrapped package graph (IWP) and the primitive, gyroid, and IWP versions of the FG-TPMS plate model. The TPMS geometry describes the properties of the sheet-based solid type [36].

$$\text{Primitive}: \ \psi(\mathscr{x},\mathscr{y},\mathscr{z}) = \cos(\chi_1\mathscr{x}) + \cos(\chi_2\mathscr{y}) + \cos(\chi_3\mathscr{z}), \tag{1a}$$

$$\text{Gyroid}: \ \psi(\mathscr{x},\mathscr{y},\mathscr{z}) = \sin(\chi_1\mathscr{x})\cos(\chi_2\mathscr{y}) + \sin(\chi_2\mathscr{y})\cos(\chi_3\mathscr{z}) + \sin(\chi_3\mathscr{z})\cos(\chi_1\mathscr{x}), \tag{1b}$$

$$IWP: \psi(\mathscr{x},\mathscr{y},\mathscr{z}) = 2(\cos(\chi_1\mathscr{x})\cos(\chi_2\mathscr{y}) + \cos(\chi_2\mathscr{y})\cos(\chi_3\mathscr{z}) + \cos(\chi_3\mathscr{z})\cos(\chi_1\mathscr{x})) - (\cos(2\chi_1\mathscr{x}) + \cos(2\chi_2\mathscr{y}) + \cos(2\chi_3\mathscr{z})). \tag{1c}$$

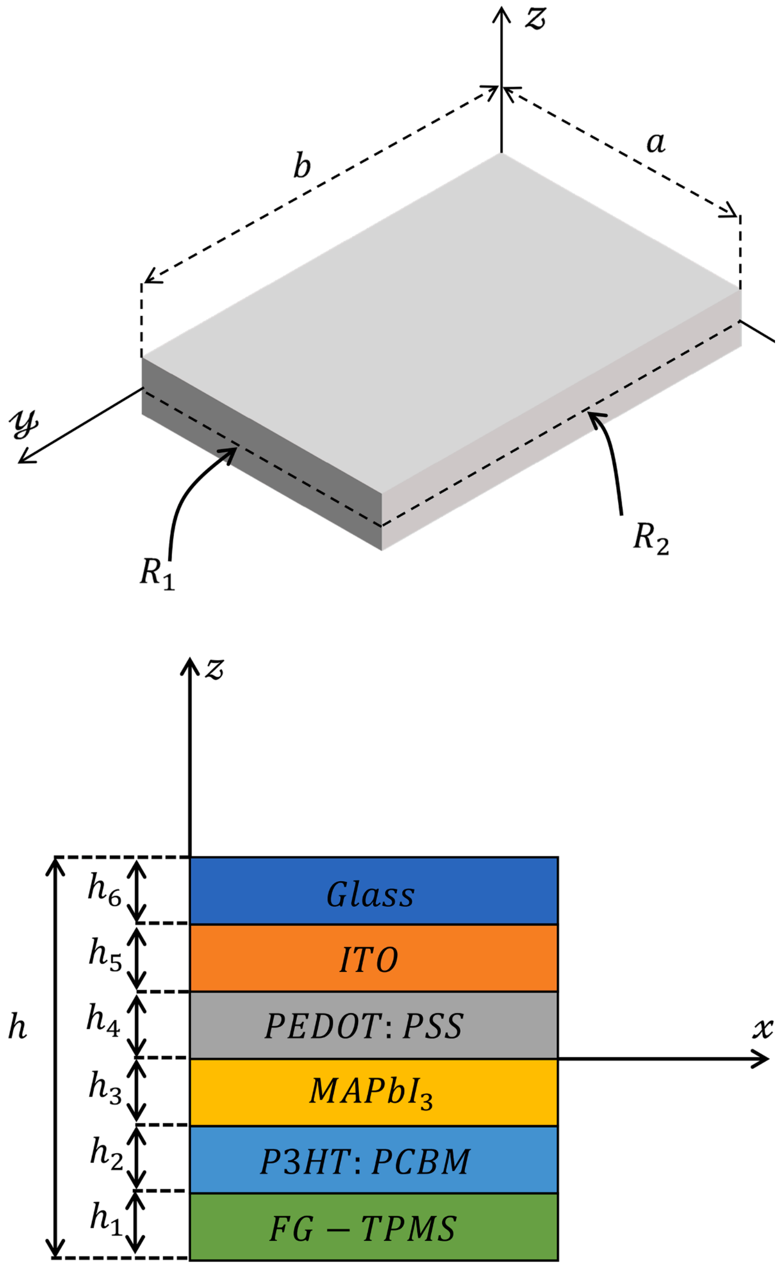

Fig. 1. 2D, and 3D representation of a multilayer perovskite solar cell.

The function $\psi(\mathcal{x},\mathcal{y},\mathcal{z})$ represents the surface and is evaluated at a constant value. This surface has a topology similar to that of a minimal surface.

$$\chi_i = \frac{2\pi n_i}{l_i}, i = 1, 2, 3. \tag{2}$$

where n_i represents the number of unit cells and l_i the relative lengths of the unit cells. This research uses readily accessible software to provide three distinct unit cell geometries (Primitive, Gyroid, and IWP) in order to increase clarity [37]. For this study, we use the curve-fitting model proposed by Nguyen-Xuan et al. [5]. In that paradigm, the volume ratio is stated as follows.

$$V = \frac{V^{TPMS}}{V^m}, \tag{3}$$

V^{TPMS} indicates the total volume of TPMS cells, while V^m indicates the total volume of the base material. Eq. (3)'s function of the volume ratio may be stated as follows:

$$V = \begin{cases} (V_{\max} - V_{\min})V_{\mathcal{z}}^{Pattern\ PA} + V_{\min} \text{ Pattern PA} \\ (V_{\max} - V_{\min})V_{\mathcal{z}}^{Pattern\ PB} + V_{\min} \text{ Pattern PB} \end{cases}, \tag{4}$$

where

$$V_{\mathcal{z}}^{\text{Pattern PA}} = \left(\frac{\mathcal{z}+\frac{h}{2}}{h_1}\right)^n \text{ and } V_{\mathcal{z}}^{\text{Pattern PB}} = \left(1 - \cos\left(\pi\left(\frac{\mathcal{z}+\frac{h}{2}}{h_1} - \frac{1}{2}\right)\right)\right)^n.$$

Treating pattern PA and pattern PB as independent functions across the thickness of the plate allows for their differentiation, as per Eq. (4). Variations in $\mathcal{z}$ and n cause a corresponding adjustment in the value of $V_{\mathcal{z}}$. Two patterns are often given different values, although these distinctions are useless. Generally speaking, the fundamental equations include those involving equilibrium, compatibility, and kinematics. The HSDT states that the strain-stress relationship may be mathematically expressed using the general version of Hooke's rule.

$$\begin{Bmatrix} \sigma_{xx} \\ \sigma_{yy} \\ \sigma_{yz} \\ \sigma_{xz} \\ \sigma_{xy} \end{Bmatrix} = \begin{bmatrix} \mathbb{C}_{11} & \mathbb{C}_{12} & 0 & 0 & 0 \\ \mathbb{C}_{21} & \mathbb{C}_{22} & 0 & 0 & 0 \\ 0 & 0 & \mathbb{C}_{44} & 0 & 0 \\ 0 & 0 & 0 & \mathbb{C}_{55} & 0 \\ 0 & 0 & 0 & 0 & \mathbb{C}_{66} \end{bmatrix} \begin{Bmatrix} \varepsilon_{xx} \\ \varepsilon_{yy} \\ \gamma_{yz} \\ \gamma_{xz} \\ \gamma_{xy} \end{Bmatrix}, \tag{5}$$

where

$$\mathbb{C}_{11} = \mathbb{C}_{22} = \frac{E_{TPMS}}{1-(\upsilon_{TPMS})^2}, \mathbb{C}_{12} = \frac{\upsilon_{TPMS} E_{TPMS}}{1-(\upsilon_{TPMS})^2}, \mathbb{C}_{66} = \mathbb{C}_{55} = \mathbb{C}_{44} = G_{TPMS}, \tag{6}$$

The symbols E_{TPMS}, G_{TPMS} and υ_{TPMS} stand for the Young's modulus, shear modulus, and Poisson's ratio of the FG-TPMS materials, respectively. The values in Table 1 were generated and provided using the fixed data model [5].

This section looks at numerical examples for each kind of FG-TPMS panel, taking into account six distinct volume distribution scenarios. Table 2 displays these scenarios, and according to Eq. (4), the $V_{average}$ value is set at 0.35. To carry out the required integration for the current method, three-node triangle cells are used, with three integrated points of 3×3 for each triangle cell. There are the following qualities of the basic ingredients: Young's modulus (E_m) is 70 [GPa], density (ρ_m) is 2702 [kg/m^3], and Poisson's ratio (ν_m) is 0.3.

Furthermore, Ref. [38] provides a list of the characteristics of the materials used to create the contemporary cantilevered solar cell.

In Table 3 we have:

As stated in the introduction, we describe the structure's kinematic field using a higher-order shear deformation theory (HSDT), i.e., [39]:

$$u(x,y,z,t) = A_x u_0(x,y,t) + z u_1(x,y,t) + z^2 u_2(x,y,t) + z^3 u_3(x,y,t), \tag{7}$$

$$v(x,y,z,t) = A_y v_0(x,y,t) + z v_1(x,y,t) + z^2 v_2(x,y,t) + z^3 v_3(x,y,t),$$

$$w(x,y,z,t) = w_0(x,y,t).$$

where $A_x = 1 + \frac{z}{R_1}$ and $A_y = 1 + \frac{z}{R_2}$. Within Eq. (7), u_0, v_0, are in-plane displacement parameters. Moreover, w_0 is the displacement of an arbitrary point (x,y) at the middle shell. Also, u_1 and v_1 are around y- and x-axes rotations respectively. u_2, v_2, u_3, and v_3 show Taylor's series of higher-order terms.

As such, the relationships between displacement and strain may be written as follows [40]:

$$\varepsilon_{xx} = \frac{1}{A_x}\left(\frac{\partial u}{\partial x} + \frac{w}{R_1}\right), \varepsilon_{yy} = \frac{1}{A_y}\left(\frac{\partial v}{\partial y} + \frac{w}{R_2}\right), \gamma_{xz} = \frac{1}{A_x}\left(\frac{\partial w}{\partial x} - \frac{u}{R_1}\right) + \frac{\partial u}{\partial z}, \tag{8}$$

$$\gamma_{yz} = \frac{\partial v}{\partial z} + \frac{1}{A_y}\left(\frac{\partial w}{\partial y} - \frac{v}{R_2}\right), \gamma_{xy} = \frac{1}{A_x}\frac{\partial v}{\partial x} + \frac{1}{A_y}\frac{\partial u}{\partial y}.$$

For the present system, the motion equations and corresponding boundary conditions (B. Cs) may be obtained using the variational energy approach as follows:

$$\int_{t_1}^{t_2} (\delta T - (\delta U + \delta W_F))dt = 0, \tag{9}$$

where kinetic energy is [40]:

$$\int\int\int_V \rho\left(\frac{\partial u}{\partial t}\frac{\partial \delta u}{\partial t} + \frac{\partial v}{\partial t}\frac{\partial \delta v}{\partial t} + \frac{\partial w}{\partial t}\frac{\partial \delta w}{\partial t}\right)dV, \tag{10}$$

In addition, the strain energy [40] connected to the current system may be expressed using the equation that follows.

$$\delta U = \int_{-h/2}^{h/2} \iint_A \Big(\sigma_{xy}\delta\gamma_{xy} + \sigma_{xx}\delta\varepsilon_{xx} + \sigma_{yy}\delta\varepsilon_{yy} + \sigma_{xz}\delta\gamma_{xz} + \sigma_{yz}\delta\gamma_{yz} + m^s_{xx}\chi^s_{xx} + m^s_{yy}\chi^s_{yy} + m^s_{zz}\chi^s_{zz} + m^s_{yz}\chi^s_{yz} + m^s_{xz}\chi^s_{xz} + m^s_{xy}\chi^s_{xy}\Big)\mathrm{dV}, \tag{11}$$

Besides, χ^s_{ij}, and m^s_{ij} can be defined as:

$$\chi^s_{ij} = \frac{1}{2}(\varphi_{i,j} + \varphi_{j,i}), \tag{12}$$

$$m^s_{ij} = 2l^2\mu\chi^s_{ij},$$

Also have:

$$\varphi = \frac{1}{2}\begin{bmatrix} i & j & k \\ \frac{\partial}{\partial x} & \frac{\partial}{\partial y} & \frac{\partial}{\partial z} \\ u & v & w \end{bmatrix}, \tag{13}$$

where:

$$\varphi_x = \frac{1}{2}\left(\frac{\partial w_0}{\partial y} - \frac{v_0}{R_2} - v_1 - 2zv_2 - 3z^2v_3\right),$$

$$\varphi_y = \frac{1}{2}\left(\frac{u_0}{R_1} + u_1 + 2zu_2 + 3z^2u_3 - \frac{\partial w_0}{\partial x}\right),$$

Table 1
Mechanical properties and characteristics of FG-TPMS materials.

TPMS	Mechanical properties	V
Primitive	$E_{TPMS} = E_m\begin{cases} 0.317V^{1.264} \\ 1.007V^{2.006} - 0.007 \end{cases}$	$V \le 0.25$ $V > 0.25$
	$G_{TPMS} = G_m\begin{cases} 0.705V^{1.189} \\ 0.953V^{1.715} + 0.047 \end{cases}$	$V \le 0.25$ $V > 0.25$
	$\upsilon_{TPMS} = \begin{cases} 0.314e^{-1.004V} + 0.119 \\ 0.152V^2 - 0.235V + 0.383 \end{cases}$	$V \le 0.55$ $V > 0.55$
Gyroid	$E_{TPMS} = E_m\begin{cases} 0.596V^{1.467} \\ 0.962V^{2.351} + 0.038 \end{cases}$	$V \le 0.45$ $V > 0.45$
	$G_{TPMS} = G_m\begin{cases} 0.777V^{1.544} \\ 0.973V^{1.982} + 0.027 \end{cases}$	$V \le 0.45$ $V > 0.45$
	$\upsilon_{TPMS} = \begin{cases} 0.192e^{-1.349V} + 0.202 \\ 0.402V^2 - 0.603V + 0.501 \end{cases}$	$V \le 0.50$ $V > 0.50$
IWP	$E_{TPMS} = E_m\begin{cases} 0.597V^{1.225} \\ 0.987V^{1.782} + 0.013 \end{cases}$	$V \le 0.35$ $V > 0.35$
	$G_{TPMS} = G_m\begin{cases} 0.529V^{1.287} \\ 0.960V^{2.188} + 0.040 \end{cases}$	$V \le 0.35$ $V > 0.35$
	$\upsilon_{TPMS} = \begin{cases} 2.597e^{-0.157V} - 2.244 \\ 0.201V^2 - 0.227V + 0.326 \end{cases}$	$V \le 0.13$ $V > 0.13$

Table 2
Six unique volume distribution patterns to take into $V_{average} = 0.35$ [5].

Parameter	PA1	PA2	PA3	PB1	PB2	PB3
n	1.0	3.0	6.5	0.561	1.757	3.943
$V_{\min}$	0.20	0.20	0.25	0.20	0.20	0.25
$V_{\max}$	0.5	0.8	1.0	0.5	0.8	1.0

Table 3
A list of the characteristics of the materials used to create the contemporary cantilevered solar cell.

Young's modulus	Poisson's ratio	Density	z
E_{TPMS}	υ_{TPMS}	ρ_{TPMS}	$-\frac{h}{2} < z < -\frac{h}{2} + h_1$
$E_{\mathrm{P3HT:\ PCBM}}$	$\upsilon_{\mathrm{P3HT:\ PCBM}}$	$\rho_{\mathrm{P3HT:\ PCBM}}$	$-\frac{h}{2} + h_1 < z < -h_3$
$E_{\mathrm{MAPbI_3}}$	$\upsilon_{\mathrm{MAPbI_3}}$	$\rho_{\mathrm{MAPbI_3}}$	$-h_3 < z < 0$
$E_{\mathrm{PDEOTL:\ PSS}}$	$\upsilon_{\mathrm{PDEOTL:\ PSS}}$	$\rho_{\mathrm{PDEOTL:\ PSS}}$	$0 < z < h_4$
E_{ITO}	υ_{ITO}	ρ_{ITO}	$h_4 < z < h_4 + h_5$
E_{Glass}	$\upsilon_{\mathrm{Glass}}$	ρ_{Glass}	$\frac{h}{2} - h_6 < z < \frac{h}{2}$

$$\varphi_z = \frac{1}{2}\left(A_y\frac{\partial v_0}{\partial x} + z\frac{\partial v_1}{\partial x} + z^2\frac{\partial v_2}{\partial x} + z^3\frac{\partial v_3}{\partial x} - A_x\frac{\partial u_0}{\partial y} - z\frac{\partial u_1}{\partial y} - z^2\frac{\partial u_2}{\partial y} - z^3\frac{\partial u_3}{\partial y}\right), \tag{14}$$

Using the equations previously presented in Eq. (12), you can:

$$\chi_{xx} = \frac{\partial \varphi_x}{\partial x} = \left(\frac{\partial^2 w_0}{\partial x \partial y} - \frac{1}{R_2}\frac{\partial v_0}{\partial x} - \frac{\partial v_1}{\partial x} - 2z\frac{\partial v_2}{\partial x} - 3z^2\frac{\partial v_3}{\partial x}\right)$$

$$\chi_{yy} = \frac{\partial \varphi_y}{\partial y} = \left(\frac{1}{R_1}\frac{\partial u_0}{\partial y} + \frac{\partial u_1}{\partial y} + 2z\frac{\partial u_2}{\partial y} + 3z^2\frac{\partial u_3}{\partial y} - \frac{\partial^2 w_0}{\partial x \partial y}\right),$$

$$\chi_{zz} = \frac{\partial \varphi_z}{\partial z} = \left(\frac{1}{R_2}\frac{\partial v_0}{\partial x} + \frac{\partial v_1}{\partial x} + 2z\frac{\partial v_2}{\partial x} + 3z^2\frac{\partial v_3}{\partial x} - \frac{1}{R_1}\frac{\partial u_0}{\partial y} - \frac{\partial u_1}{\partial y} - 2z\frac{\partial u_2}{\partial y} - 3z^2\frac{\partial u_3}{\partial y}\right),$$

$$2\chi_{yz} = \frac{\partial \varphi_y}{\partial z} + \frac{\partial \varphi_z}{\partial y} = (2u_2 + 6zu_3) + \left(A_y\frac{\partial^2 v_0}{\partial x\partial y} + z\frac{\partial^2 v_1}{\partial x\partial y} + z^2\frac{\partial^2 v_2}{\partial x\partial y} + z^3\frac{\partial^2 v_3}{\partial x\partial y} - A_x\frac{\partial^2 u_0}{\partial y^2} - z\frac{\partial^2 u_1}{\partial y^2} - z^2\frac{\partial^2 u_2}{\partial y^2} - z^3\frac{\partial^2 u_3}{\partial y^2}\right),$$

$$2\chi_{xz} = \frac{\partial \varphi_x}{\partial z} + \frac{\partial \varphi_z}{\partial x} = (-2v_2 - 6zv_3) + \left(A_y\frac{\partial^2 v_0}{\partial x^2} + z\frac{\partial^2 v_1}{\partial x^2} + z^2\frac{\partial^2 v_2}{\partial x^2} + z^3\frac{\partial^2 v_3}{\partial x^2} - A_x\frac{\partial^2 u_0}{\partial x\partial y} - z\frac{\partial^2 u_1}{\partial x\partial y} - z^2\frac{\partial^2 u_2}{\partial x\partial y} - z^3\frac{\partial^2 u_3}{\partial x\partial y}\right),$$

$$2\chi_{xy} = \frac{\partial \varphi_x}{\partial y} + \frac{\partial \varphi_y}{\partial x} = \left(\frac{\partial^2 w_0}{\partial y^2} - \frac{1}{R_2}\frac{\partial v_0}{\partial y} - \frac{\partial v_1}{\partial y} - 2z\frac{\partial v_2}{\partial y} - 3z^2\frac{\partial v_3}{\partial y}\right) + \left(\frac{1}{R_1}\frac{\partial u_0}{\partial x} + \frac{\partial u_1}{\partial x} + 2z\frac{\partial u_2}{\partial x} + 3z^2\frac{\partial u_3}{\partial x} - \frac{\partial^2 w_0}{\partial x^2}\right), \tag{15}$$

Furthermore, the work that the elastic substrate does would be determined by the following:

$$W_F = \frac{1}{2}\int [-K_W w] w dA, \tag{16}$$

K_W is the Winkler coefficient of the substrate. Additionally, the definition of the variation of Eq. (16) is provided below.

$$\delta W_F = \int [-K_W w] \delta w dA, \tag{17}$$

The motion equations of the current system are then found by modifying Eq. (9) to include Eqs. (10), (11), and (17) as well:

$$\delta u_0 : \frac{\partial \mathbb{N}^*_{xx}}{\partial x} + \frac{\mathbb{N}_{xz}}{R_1} - \frac{\mathbb{N}^*_{xz}}{R_1} + \frac{\partial \mathbb{N}^y_{xy}}{\partial y} + \frac{1}{R_1}\frac{\partial \mathbb{N}^{(0)}_{yy}}{\partial y} - \frac{1}{R_1}\frac{\partial \mathbb{N}^{(0)}_{zz}}{\partial y} + \frac{1}{2}\frac{\partial^2 \mathbb{N}^{*(0)}_{yz}}{\partial y^2} + \frac{1}{2}\frac{\partial^2 \mathbb{N}^{*(0)}_{xz}}{\partial x\partial y} + \frac{1}{2R_1}\frac{\partial \mathbb{N}^{(0)}_{xy}}{\partial x} = \mathbb{J}^x_0\frac{\partial^2 u_0}{\partial t^2} + \mathbb{J}^x_1\frac{\partial^2 u_1}{\partial t^2} + \mathbb{J}^x_2\frac{\partial^2 u_2}{\partial t^2} + \mathbb{J}^x_3\frac{\partial^2 u_3}{\partial t^2}, \tag{18a}$$

$$\delta v_0 : \frac{\partial \mathbb{N}^*_{yy}}{\partial y} + \frac{\mathbb{N}_{yz}}{R_2} - \frac{\mathbb{N}^*_{yz}}{R_2} + \frac{\partial \mathbb{N}^x_{xy}}{\partial x} - \frac{1}{R_2}\frac{\partial \mathbb{N}^{(0)}_{xx}}{\partial x} + \frac{1}{R_2}\frac{\partial \mathbb{N}^{(0)}_{zz}}{\partial x} - \frac{1}{2}\frac{\partial^2 \mathbb{N}^{*(0)}_{yz}}{\partial x\partial y} - \frac{1}{2}\frac{\partial^2 \mathbb{N}^{*(0)}_{xz}}{\partial x^2} - \frac{1}{2R_2}\frac{\partial \mathbb{N}^{(0)}_{xy}}{\partial y} = \mathbb{J}^y_0\frac{\partial^2 v_0}{\partial t^2} + \mathbb{J}^y_1\frac{\partial^2 v_1}{\partial t^2} + \mathbb{J}^y_2\frac{\partial^2 v_2}{\partial t^2} + \mathbb{J}^y_3\frac{\partial^2 v_3}{\partial t^2}, \tag{18b}$$

$$\delta w_0 : -\left(\frac{\mathbb{N}_{xx}}{R_1} + \frac{\mathbb{N}_{yy}}{R_2}\right) + \frac{\partial \mathbb{N}_{xz}}{\partial x} + \frac{\partial \mathbb{N}_{yz}}{\partial y} - \frac{\partial^2 \mathbb{N}^{(0)}_{xx}}{\partial x\partial y} + \frac{\partial^2 \mathbb{N}^{(0)}_{yy}}{\partial x\partial y} - \frac{1}{2}\frac{\partial^2 \mathbb{N}^{(0)}_{xy}}{\partial y^2} + \frac{1}{2}\frac{\partial^2 \mathbb{N}^{(0)}_{xy}}{\partial x^2} - K_W w_0 = \mathbb{J}^z_0\frac{\partial^2 w_0}{\partial t^2}, \tag{18c}$$

$$\delta u_1 : \frac{\partial \mathbb{M}_{xx}}{\partial x} + \frac{\mathbb{M}_{xz}}{R_1} - \mathbb{N}^*_{xz} + \frac{\partial \mathbb{M}^y_{xy}}{\partial y} + \frac{\partial \mathbb{N}^{(0)}_{yy}}{\partial y} - \frac{\partial \mathbb{N}^{(0)}_{zz}}{\partial y} + \frac{1}{2}\frac{\partial^2 \mathbb{M}^{(0)}_{yz}}{\partial y^2} + \frac{1}{2}\frac{\partial^2 \mathbb{M}^{(0)}_{xz}}{\partial x\partial y} + \frac{1}{2}\frac{\partial \mathbb{N}^{(0)}_{xy}}{\partial x} = \mathbb{J}^x_0\frac{\partial^2 u_0}{\partial t^2} + \mathbb{J}^x_1\frac{\partial^2 u_1}{\partial t^2} + \mathbb{J}^x_2\frac{\partial^2 u_2}{\partial t^2} + \mathbb{J}^x_3\frac{\partial^2 u_3}{\partial t^2}, \tag{18d}$$

$$\delta v_1 : \frac{\partial \mathbb{M}_{yy}}{\partial y} + \frac{\mathbb{M}_{yz}}{R_2} - \mathbb{N}^*_{yz} + \frac{\partial \mathbb{M}^x_{xy}}{\partial x} - \frac{\partial \mathbb{N}^{(0)}_{xx}}{\partial x} + \frac{\partial \mathbb{N}^{(0)}_{zz}}{\partial x} - \frac{1}{2}\frac{\partial^2 \mathbb{M}^{(0)}_{yz}}{\partial x\partial y} - \frac{1}{2}\frac{\partial^2 \mathbb{M}^{(0)}_{xz}}{\partial x^2} - \frac{1}{2}\frac{\partial \mathbb{N}^{(0)}_{xy}}{\partial y} = \mathbb{J}^y_0\frac{\partial^2 v_0}{\partial t^2} + \mathbb{J}^y_1\frac{\partial^2 v_1}{\partial t^2} + \mathbb{J}^y_2\frac{\partial^2 v_2}{\partial t^2} + \mathbb{J}^y_3\frac{\partial^2 v_3}{\partial t^2}, \tag{18e}$$

$$\delta u_2 : \frac{\partial \mathbb{P}_{xx}}{\partial x} + \frac{\mathbb{P}_{xz}}{R_1} - 2\mathbb{M}^*_{xz} + \frac{\partial \mathbb{P}^y_{xy}}{\partial y} + 2\frac{\partial \mathbb{M}^{(0)}_{yy}}{\partial y} - 2\frac{\partial \mathbb{M}^{(0)}_{zz}}{\partial y} - \mathbb{N}^{(0)}_{yz} + \frac{1}{2}\frac{\partial^2 \mathbb{P}^{(0)}_{yz}}{\partial y^2} + \frac{1}{2}\frac{\partial^2 \mathbb{P}^{(0)}_{xz}}{\partial x\partial y} + \frac{\partial \mathbb{M}^{(0)}_{xy}}{\partial x} = \mathbb{K}^x_0\frac{\partial^2 u_0}{\partial t^2} + \mathbb{K}^x_1\frac{\partial^2 u_1}{\partial t^2} + \mathbb{K}^x_2\frac{\partial^2 u_2}{\partial t^2} + \mathbb{K}^x_3\frac{\partial^2 u_3}{\partial t^2}, \tag{18f}$$

$$\delta v_2 : \frac{\partial \mathbb{P}_{yy}}{\partial y} + \frac{\mathbb{P}_{yz}}{R_2} - 2\mathbb{M}^*_{yz} + \frac{\partial \mathbb{P}^x_{xy}}{\partial x} - 2\frac{\partial \mathbb{M}^{(0)}_{xx}}{\partial x} + 2\frac{\partial \mathbb{M}^{(0)}_{zz}}{\partial x} + \mathbb{N}^{(0)}_{xz} - \frac{1}{2}\frac{\partial^2 \mathbb{P}^{(0)}_{yz}}{\partial x\partial y} - \frac{1}{2}\frac{\partial^2 \mathbb{P}^{(0)}_{xz}}{\partial x^2} - \frac{\partial \mathbb{M}^{(0)}_{xy}}{\partial y} = \mathbb{K}^y_0\frac{\partial^2 v_0}{\partial t^2} + \mathbb{K}^y_1\frac{\partial^2 v_1}{\partial t^2} + \mathbb{K}^y_2\frac{\partial^2 v_2}{\partial t^2} + \mathbb{K}^y_3\frac{\partial^2 v_3}{\partial t^2}, \tag{18g}$$

$$\delta u_3 : \frac{\partial \mathbb{Q}_{xx}}{\partial x} + \frac{\mathbb{Q}_{xz}}{R_1} - 3\mathbb{P}^*_{xz} + \frac{\partial \mathbb{Q}^y_{xy}}{\partial y} + 3\frac{\partial \mathbb{P}^{(0)}_{yy}}{\partial y} - 3\frac{\partial \mathbb{P}^{(0)}_{zz}}{\partial y} - 3\mathbb{M}^{(0)}_{yz} + \frac{1}{2}\frac{\partial^2 \mathbb{Q}^{(0)}_{yz}}{\partial y^2} + \frac{1}{2}\frac{\partial^2 \mathbb{Q}^{(0)}_{xz}}{\partial x\partial y} + \frac{3}{2}\frac{\partial \mathbb{P}^{(0)}_{xy}}{\partial x} = \mathbb{L}^x_0\frac{\partial^2 u_0}{\partial t^2} + \mathbb{L}^x_1\frac{\partial^2 u_1}{\partial t^2} + \mathbb{L}^x_2\frac{\partial^2 u_2}{\partial t^2} + \mathbb{L}^x_3\frac{\partial^2 u_3}{\partial t^2}, \tag{18h}$$

$$\delta v_3 : \frac{\partial \mathbb{Q}_{yy}}{\partial y} + \frac{\mathbb{Q}_{yz}}{R_2} - 3\mathbb{P}^*_{yz} + \frac{\partial \mathbb{Q}^x_{xy}}{\partial x} - 3\frac{\partial \mathbb{P}^{(0)}_{xx}}{\partial x} + 3\frac{\partial \mathbb{P}^{(0)}_{zz}}{\partial x} + 3\mathbb{M}^{(0)}_{xz} - \frac{1}{2}\frac{\partial^2 \mathbb{Q}^{(0)}_{yz}}{\partial x\partial y} - \frac{1}{2}\frac{\partial^2 \mathbb{Q}^{(0)}_{xz}}{\partial x^2} - \frac{3}{2}\frac{\partial \mathbb{P}^{(0)}_{xy}}{\partial y} = \mathbb{L}^y_0\frac{\partial^2 v_0}{\partial t^2} + \mathbb{L}^y_1\frac{\partial^2 v_1}{\partial t^2} + \mathbb{L}^y_2\frac{\partial^2 v_2}{\partial t^2} + \mathbb{L}^y_3\frac{\partial^2 v_3}{\partial t^2}, \tag{18i}$$

In which:

$$\int_V dV = \iint_A \int_{-\frac{h}{2}}^{\frac{h}{2}} dz dA$$

$$= \iint_A \int_{-\frac{h}{2}}^{-\frac{h}{2}+h_1} dz dA + \iint_A \int_{-\frac{h}{2}+h_1}^{-h_3} dz dA + \iint_A \int_{-h_3}^{0} dz dA$$

$$+ \iint_A \int_{0}^{h_4} dz dA + \iint_A \int_{h_4}^{h_4+h_5} dz dA + \iint_A \int_{\frac{h}{2}-h_6}^{\frac{h}{2}} dz dA.$$

$$\{\mathbb{N}^*_{xx}, \mathbb{N}_{xx}, \mathbb{M}_{xx}, \mathbb{P}_{xx}, \mathbb{Q}_{xx}\} = \int_V \frac{1}{A_x}\{A_x, 1, z, z^2, z^3\}\sigma_{xx} dV,$$

$$\left\{\mathbb{N}^*_{yy}, \mathbb{N}_{yy}, \mathbb{M}_{yy}, \mathbb{P}_{yy}, \mathbb{Q}_{yy}\right\} = \int_V \frac{1}{A_y}\{A_y, 1, z, z^2, z^3\}\sigma_{yy} dV,$$

$$\{\mathbb{N}_{xz}, \mathbb{M}_{xz}, \mathbb{P}_{xz}, \mathbb{Q}_{xz}\} = \int_V \frac{1}{A_x}\{1, z, z^2, z^3\}\sigma_{xz} dV,$$

$$\{\mathbb{N}_{yz}, \mathbb{M}_{yz}, \mathbb{P}_{yz}, \mathbb{Q}_{yz}\} = \int_V \frac{1}{A_y}\{1, z, z^2, z^3\}\sigma_{yz} dV,$$

$$\left\{\mathbb{N}^x_{xy}, \mathbb{M}^x_{xy}, \mathbb{P}^x_{xy}, \mathbb{Q}^x_{xy}\right\} = \int_V \frac{1}{A_x}\{A_y, z, z^2, z^3\}\sigma_{xy} dV,$$

$$\{\mathbb{N}^*_{xz}, \mathbb{M}^*_{xz}, \mathbb{P}^*_{xz}\} = \int_V \{1, z, z^2\}\sigma_{xz} dV,$$

$$\left\{\mathbb{N}^*_{yz}, \mathbb{M}^*_{yz}, \mathbb{P}^*_{yz}\right\} = \int_V \{1, z, z^2\}\sigma_{yz} dV,$$

$$\left\{\mathbb{N}^y_{xy}, \mathbb{M}^y_{xy}, \mathbb{P}^y_{xy}, \mathbb{Q}^y_{xy}\right\} = \int_V \frac{1}{A_y}\{A_x, z, z^2, z^3\}\sigma_{xy} dV,$$

$$\left\{\mathbb{N}^{(0)}_{ij}, \mathbb{M}^{(0)}_{ij}, \mathbb{P}^{(0)}_{ij}, \mathbb{Q}^{(0)}_{ij}\right\} = \int_V \{1, z, z^2, z^3\} m_{ij} dV i, j = x, y, z.$$

$$\{\mathbb{J}^x_0, \mathbb{J}^x_1, \mathbb{J}^x_2, \mathbb{J}^x_3\} = \int_V A_x \rho\{A_x, z, z^2, z^3\} dV,$$

$$\{\mathcal{I}^x_0, \mathcal{I}^x_1, \mathcal{I}^x_2, \mathcal{I}^x_3\} = \int_V \rho\{z A_x, z^2, z^3, z^4\} dV,$$

$$\{\mathbb{K}^x_0, \mathbb{K}^x_1, \mathbb{K}^x_2, \mathbb{K}^x_3\} = \int_V \rho\{z^2 A_x, z^3, z^4, z^5\} dV,$$

$$\{\mathbb{L}^x_0, \mathbb{L}^x_1, \mathbb{L}^x_2, \mathbb{L}^x_3\} = \int_V \rho\{z^3 A_x, z^4, z^5, z^6\} dV,$$

$$\{\mathbb{J}^y_0, \mathbb{J}^y_1, \mathbb{J}^y_2, \mathbb{J}^y_3\} = \int_V A_y \rho\{A_y, z, z^2, z^3\} dV,$$

$$\{\mathcal{I}^y_0, \mathcal{I}^y_1, \mathcal{I}^y_2, \mathcal{I}^y_3\} = \int_V \rho\{z A_y, z^2, z^3, z^4\} dV,$$

$$\{\mathbb{K}^y_0, \mathbb{K}^y_1, \mathbb{K}^y_2, \mathbb{K}^y_3\} = \int_V \rho\{z^2 A_y, z^3, z^4, z^5\} dV,$$

$$\{\mathbb{L}^y_0, \mathbb{L}^y_1, \mathbb{L}^y_2, \mathbb{L}^y_3\} = \int_V \rho\{z^3 A_y, z^4, z^5, z^6\} dV,$$

$$\{\mathbb{J}^z_0\} = \int_V \rho dV. \quad (19)$$

3. Solution procedure

This paper employs an analytical technique to deduce vibration modes using trigonometric functions. The following series are used to estimate the curvilinear and normal displacements and satisfy the required simply supported conditions at each edge of the microsystem.

$$u_0 = \sum_{m=1}^{\infty} \sum_{n=1}^{\infty} \mathfrak{u}_{0mn} cos(\alpha x) sin(\beta y) exp(i\Omega t), \quad (20a)$$

$$v_0 = \sum_{m=1}^{\infty} \sum_{n=1}^{\infty} \mathfrak{v}_{0mn} sin(\alpha x) cos(\beta y) exp(i\Omega t), \quad (20b)$$

$$w_0 = \sum_{m=1}^{\infty} \sum_{n=1}^{\infty} \mathfrak{w}_{0mn} sin(\alpha x) sin(\beta y) exp(i\Omega t), \quad (20c)$$

$$u_1 = \sum_{m=1}^{\infty} \sum_{n=1}^{\infty} \mathfrak{u}_{1mn} cos(\alpha x) sin(\beta y) exp(i\Omega t), \quad (20d)$$

$$v_1 = \sum_{m=1}^{\infty} \sum_{n=1}^{\infty} \mathfrak{v}_{1mn} sin(\alpha x) cos(\beta y) exp(i\Omega t), \quad (20e)$$

$$u_2 = \sum_{m=1}^{\infty} \sum_{n=1}^{\infty} \mathfrak{u}_{2mn} cos(\alpha x) sin(\beta y) exp(i\Omega t), \quad (20f)$$

$$v_2 = \sum_{m=1}^{\infty} \sum_{n=1}^{\infty} \mathfrak{v}_{2mn} sin(\alpha x) cos(\beta y) exp(i\Omega t), \quad (20g)$$

$$u_3 = \sum_{m=1}^{\infty} \sum_{n=1}^{\infty} \mathfrak{u}_{3mn} cos(\alpha x) sin(\beta y) exp(i\Omega t), \quad (20h)$$

$$v \quad {}_{m=1}^{\infty} \sum_{n=1}^{\infty} \mathfrak{v}_{3mn} sin(\alpha x) cos(\beta y) exp(i\Omega t). \quad (20i)$$

where $\mathfrak{u}_{0mn}$, $\mathfrak{v}_{0mn}$, $\mathfrak{w}_{0mn}$, $\mathfrak{u}_{1mn}$, $\mathfrak{v}_{1mn}$, $\mathfrak{u}_{2mn}$, $\mathfrak{v}_{2mn}$, $\mathfrak{u}_{3mn}$, $\mathfrak{v}_{3mn}$ are the amplitude components and $\alpha = m\pi/a$, $\beta = n\pi/b$, and Ω is the natural frequency. By entering Eqs. (20a-i) into the partial differential equations Eqs. (18a-i) and satisfying the non-trivial solution condition, the natural frequencies may be obtained. Furthermore, dimensionless quantities are defined as follows:

$$\omega^* = 100\Omega h^2 \sqrt{\rho_m / E_m}$$

$$K^*_W = \frac{K_W a^2}{E_m I} \quad (21)$$

4. Utilizing the SVM-DNN-GA algorithm to determine the natural frequency of enhanced perovskites cells using mathematical modeling datasets

Machine learning algorithms are crucial in predicting the mechanical properties of structures due to their ability to analyze vast amounts of data and identify complex patterns that traditional methods might miss [41,42]. These algorithms can significantly reduce the time and cost associated with experimental testing by providing accurate predictions based on computational models [43,44]. They also enhance the ability to optimize material properties and structural designs, leading to improved performance and safety [45,46]. Additionally, machine learning can adapt to new data, continuously improving its predictive accuracy over time [47]. This adaptability and efficiency make machine learning an invaluable tool in modern engineering and materials science [48,49]. The SVM-DNN-GA algorithm combines the strengths of SVM-DNN-GA, leading to enhanced predictive accuracy compared to using DNN alone. SVMs contribute to effective data classification and handling non-linear relationships, improving the initial feature selection. The integration of GAs helps in optimizing the hyperparameters and structure of the DNN, ensuring a more efficient search for the best model configuration. This hybrid approach also mitigates the risk of overfitting, a common issue in standalone DNNs, by incorporating regularization and evolutionary strategies. Overall, the SVM-DNN-GA algorithm benefits from a robust, adaptive learning process, yielding better generalization and performance in various applications.

The estimation of natural frequencies is crucial for assessing the structural integrity and dynamic performance of improved perovskite solar cells. Traditional methods can be computationally intensive and time-consuming. The integration of an innovative algorithm combining SVM-DNN-GA offers a powerful solution for this challenge.

Support Vector Machine (SVM): SVM is employed to preprocess the data and identify the most relevant features that influence the natural frequency. By classifying and selecting significant parameters from the dataset, SVM reduces the dimensionality and enhances the efficiency of subsequent modeling processes.

Deep Neural Network (DNN): With the refined dataset, DNN is utilized to model the complex, non-linear relationships between the

```
% Load dataset; data = readmatrix;
inputs = data(:, 1:end-1);
targets = data(:, end);
% Split the data into training and testing sets
cv = cvpartition(size(data,1),'HoldOut',0.3);
trainInputs = inputs(training(cv), :);
trainTargets = targets(training(cv));
testInputs = inputs(test(cv), :);
testTargets = targets(test(cv));
% Step 1: Feature Selection using SVM
svmModel = fitcsvm(trainInputs, trainTargets, 'KernelFunction', 'linear', 'Standardize', true);
[selectedFeatures, ~] = rankfeatures(trainInputs', trainTargets);
N = 10; % Adjust based on your dataset
trainInputs = trainInputs(:, selectedFeatures(1:N));
testInputs = testInputs(:, selectedFeatures(1:N));
% Step 2: Define the DNN architecture
layers = [featureInputLayer(N)
  fullyConnectedLayer(50)
  reluLayer
  fullyConnectedLayer(20)
  reluLayer
  fullyConnectedLayer(1)
  regressionLayer];
options = trainingOptions('adam', ...
  'MaxEpochs', 100, ...
  'InitialLearnRate', 0.001, ...
  'ValidationFrequency', 30, ...
  'Plots', 'training-progress', ...
  'Verbose', false);
% Train the DNN model
net = trainNetwork(trainInputs, trainTargets,
layers, options);
% Step 3: Optimize DNN hyperparameters using
GA
function mse = dnnFitnessFcn(params,
trainInputs, trainTargets, N)
  layers = [
    featureInputLayer(N)
    fullyConnectedLayer(round(params(1)))
    reluLayer
    fullyConnectedLayer(round(params(2)))
    reluLayer
    fullyConnectedLayer(1)
    regressionLayer];
  options = trainingOptions('adam', ...
    'MaxEpochs', 50, ...
    'InitialLearnRate', params(3), ...
    'ValidationFrequency', 30, ...
    'Verbose', false);
  net = trainNetwork(trainInputs, trainTargets,
layers, options);
  predictions = predict(net, trainInputs);
  mse = mean((predictions - trainTargets).^2);
end
% GA options
gaOptions = optimoptions('ga', ...
  'PopulationSize', 20, ...
  'MaxGenerations', 30, ...
  'Display', 'iter');
% [numHiddenUnits1, numHiddenUnits2,
learnRate]
lb = [10, 10, 0.0001];
ub = [100, 100, 0.01];
params = ga(@(params) dnnFitnessFcn(params,
trainInputs, trainTargets, N), 3, [], [], [], [], lb, ub,
[], gaOptions);
% Train the optimized DNN model
layers = [
  featureInputLayer(N)
  fullyConnectedLayer(round(params(1)))
  reluLayer
  fullyConnectedLayer(round(params(2)))
  reluLayer
  fullyConnectedLayer(1)
  regressionLayer];
```

Fig. 2. A MATLAB code that demonstrates the integration of SVM-DNN-GA algorithm to estimate the natural frequency of improved perovskite solar cells using mathematical datasets.

input parameters and the natural frequency of perovskite solar cells. The deep layers of the neural network enable it to capture intricate patterns and interactions within the data, providing accurate and robust predictions of natural frequencies.

Genetic Algorithm (GA): GA optimizes the hyperparameters of the DNN to ensure the best performance. It simulates the process of natural evolution, iteratively selecting, mutating, and recombining candidate solutions to converge on the optimal set of hyperparameters. This step enhances the predictive accuracy and generalization capability of the DNN model.

Mathematical Modeling Dataset: The dataset comprises simulated data generated from mathematical models of perovskite solar cells. These models incorporate various factors such as material properties, geometric configurations, and boundary conditions that affect the natural frequency. The dataset serves as a comprehensive source of information for training and validating the SVM-DNN-GA algorithm.

4.1. Application Process

1. **Data Collection and Preprocessing**: Gather extensive data from mathematical models simulating the natural frequency of perovskite solar cells. Apply SVM to preprocess the data, selecting the most relevant features.
2. **Model Training**: Use the refined dataset to train the DNN. Initialize the DNN with a broad set of hyperparameters.
3. **Optimization**: Apply GA to optimize the hyperparameters of the DNN. The GA iteratively improves the model by selecting the best-performing sets of hyperparameters.
4. **Validation and Testing**: Validate the optimized DNN model using a separate portion of the dataset. Test the model's predictive accuracy and refine it as needed.
5. **Implementation**: Use the trained and optimized model to estimate the natural frequency of new or modified perovskite solar cells, ensuring accurate and reliable predictions.

4.2. Benefits

Efficiency: The combined SVM-DNN-GA approach significantly reduces computation time compared to traditional methods.

Accuracy: The deep learning component captures complex relationships in the data, leading to precise frequency estimations.

Optimization: GA ensures that the DNN model operates with optimal hyperparameters, enhancing its performance.

Versatility: The model can adapt to various configurations and material properties of perovskite solar cells.

This innovative algorithmic approach not only improves the accuracy of natural frequency estimations but also streamlines the process, making it highly applicable for engineering and design optimizations in perovskite solar cell technology.

Fig. 2 is a MATLAB code that demonstrates the integration of SVM-DNN-GA algorithm to estimate the natural frequency of improved perovskite solar cells using mathematical datasets. Key Steps of this algorithm are as follows:

Table 4
Comparison of dimensionless fundamental frequency for doubly-curved shells ($a/b = 1$, $a/h = 10$).

R_2/R_1	Source	R_1/a				
		3	5	10	20	100
1	Kiani et al. [50]	6.5834	6.0767	5.8479	5.7891	5.7701
	Present	6.6193	6.0909	5.8516	5.7900	5.7702
	Shen et al. [51]	6.6510	6.1015	5.8542	5.7908	5.7703
2	Kiani et al. [50]	6.2330	5.9412	5.8128	5.7802	5.7698
	Present	6.2591	5.9511	5.8154	5.7809	5.7698
	Shen et al. [51]	6.2806	5.9585	5.8173	5.7815	5.7699

1. Data Loading and Preprocessing: Load the dataset, split it into training and testing sets.
2. Feature Selection using SVM: Use SVM to rank and select the top N features.
3. Define and Train Initial DNN: Define a DNN architecture and train it using the selected features.
4. Optimize Hyperparameters using GA: Optimize the DNN's hyperparameters (number of neurons in hidden layers and learning rate) using a genetic algorithm.
5. Train the Optimized DNN: Train the DNN again using the optimized hyperparameters.
6. Test the Model: Predict the natural frequency on the test dataset and calculate the mean squared error (MSE).

5. Results and discussion

In this section, first, a verification between the results of the current study and those or published articles in the literature is presented. Then in the next subsection, the mathematical modeling results are presented. In the last subsection, the outcomes of the presented hybrid machine-learning algorithm are investigated in detail.

5.1. Validation

Table 4 presents a comparison of dimensionless fundamental frequencies for doubly-curved shells with the parameters $a/b = 1$ and $a/b = 10$. The table is organized to show the results from three sources: Kiani et al. [50], the present study, and Shen et al. [51]. The columns in the table are divided based on the R_1/a ratio, which takes the values of 3, 5, 10, 20, and 100. Additionally, the results are categorized under two different ratios of R_2/R_1, specifically 1 and 2. For $R_2/R_1 = 1$, the fundamental frequencies reported by Kiani et al. are slightly different from those reported in the present study and Shen et al. [51]. For instance, at $R_1/a = 3$, Kiani et al. [50] report a frequency of 6.5834, the present study reports 6.6193, and Shen et al. [51] report 6.6510. Similar variations can be seen across other values of R_1/a. For $R_2/R_1 = 2$, the pattern remains, where slight differences exist among the three sources. For instance, at R_1/a=3, Kiani et al. [50] report 6.2330, the present study reports 6.2591, and Shen et al. [51] report 6.2806. Overall, while the frequencies reported by the three sources are close to each other, minor discrepancies are observed, which might be due to different modeling approaches or computational methods.

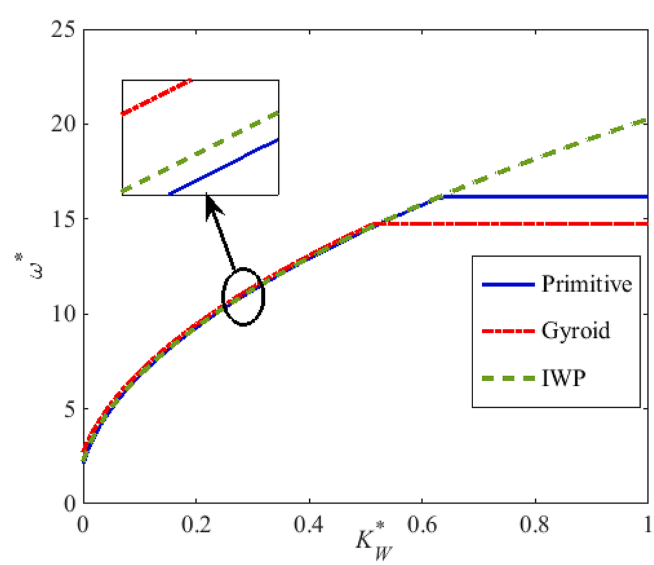

Fig. 3. Dimensionless frequency of the improved solar cell structure for various TPMS architectures and dimensionless Winkler coefficients.

5.2. Parametric results

Fig. 3 shows the relationship between the dimensionless frequency parameter (ω^*) and the dimensionless Winkler coefficient parameter (K_W^*) for three different architectures of the triply periodic minimal surface material: Primitive, Gyroid, and IWP. The x-axis represents the dimensionless Winkler coefficient parameter, which quantifies the stiffness of the elastic foundation supporting the structure. The y-axis represents the dimensionless frequency parameter, indicating the vibrational frequency of the material. The blue line represents the dimensionless frequency response of the Primitive architecture. It starts at a lower frequency and shows a steady increase with increasing K_W^*, indicating a linear relationship. The red dashed line represents the Gyroid architecture. This curve starts higher on the frequency axis compared to the Primitive architecture and shows a similar trend, but with a higher overall frequency. The green dashed line represents the IWP architecture. This line starts even higher than the Gyroid architecture and follows a similar trend, indicating the highest frequency response among the three architectures. The inset plot zooms in on a specific region where K_W^* is around 0.2. This magnified view highlights the differences in frequency responses of the three architectures more clearly. It shows that in this region, the Gyroid and IWP architectures have significantly higher frequencies compared to the Primitive architecture. This comparison is crucial for understanding how different architectural designs affect the vibrational properties of materials. The figure demonstrates that the Primitive architecture, with its simpler geometry, exhibits lower frequencies, while the more complex geometries of the Gyroid and IWP architectures result in higher frequencies. This information is essential for applications where specific vibrational properties are desired. For example, if a higher frequency response is needed, the Gyroid or IWP architecture would be preferable. Conversely, for applications requiring lower frequencies, the Primitive architecture would be more suitable. By examining these relationships, engineers and designers can select the appropriate architecture based on the specific performance requirements of their applications. This figure provides a clear visual representation of how the dimensionless Winkler coefficient influences the dimensionless frequency across different material architectures, aiding in the material selection and design process.

Fig. 4 shows the relationship between the dimensionless frequency parameter and the dimensionless Winkler coefficient parameter for different values of the R_1/a ratio. The x-axis represents the dimensionless Winkler coefficient parameter, which quantifies the stiffness of the elastic foundation supporting the structure. The y-axis represents the dimensionless frequency parameter, indicating the vibrational frequency of the material. The blue line represents the case where $R_1/a = 0.5$. This curve starts at a lower frequency and shows a gradual increase with increasing K_W^*, demonstrating how the frequency response evolves with the Winkler coefficient. The red dashed line corresponds to $R_1/a = 1$. This curve starts higher on the frequency axis compared to the $R_1/a = 0.5$ case and follows a similar increasing trend, but at a higher frequency range. The green dashed line represents $R_1/a = 1.5$. This curve also starts higher and shows a similar increasing trend, situated above the red dashed line. The purple dashed line indicates $R_1/a = 2$, starting even higher on the frequency axis and continuing the trend of increasing frequency with K_W^*. The figure clearly illustrates that as the R_1/a ratio increases, the dimensionless frequency also increases for a given value of the dimensionless Winkler coefficient. This indicates that higher values of R_1/a lead to stiffer and more

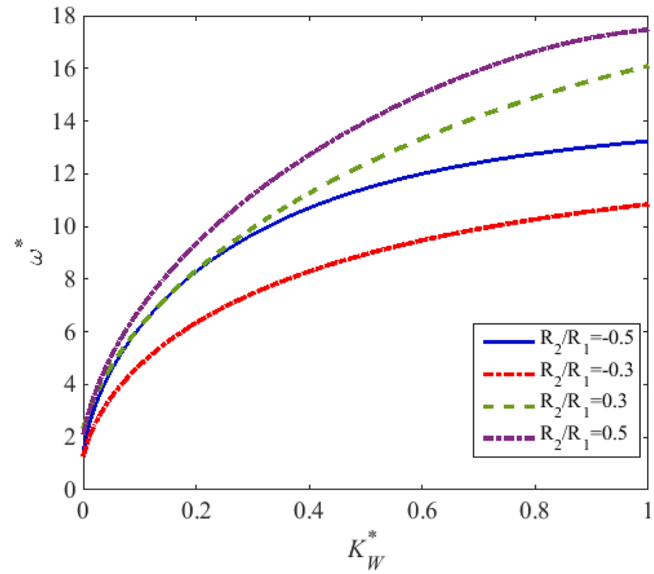

Fig. 5. Dimensionless frequency of the improved solar cell structure for various R_2/R_1 values and dimensionless Winkler coefficients.

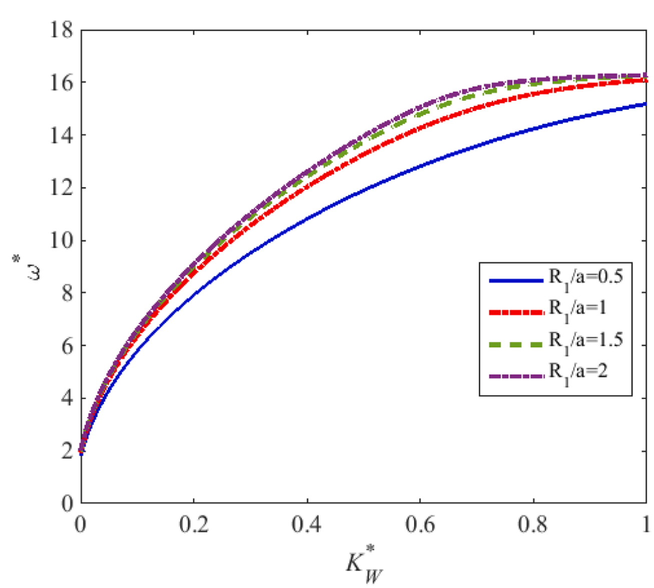

Fig. 4. Dimensionless frequency of the improved solar cell structure for various R_1/a values and dimensionless Winkler coefficients.

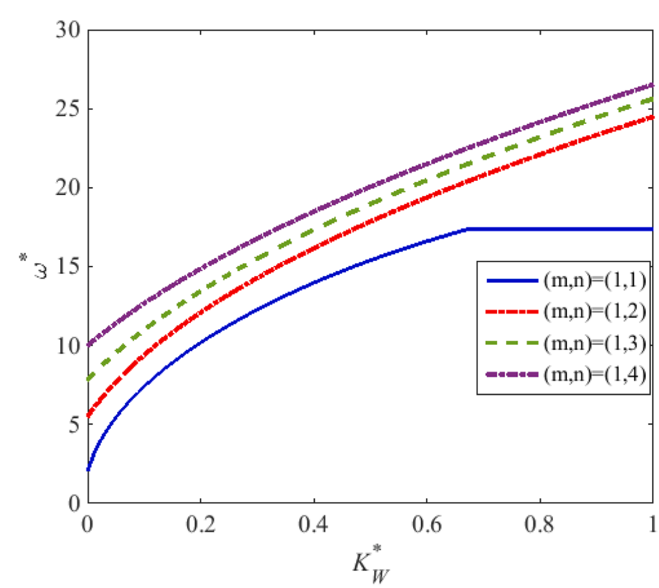

Fig. 6. Dimensionless frequency of the improved solar cell structure for various (m, n) values and dimensionless Winkler coefficients.

responsive structures in terms of vibrational behavior. This relationship is crucial for understanding how changes in structural parameters affect the vibrational properties of the material. By analyzing these trends, engineers and designers can optimize the material's performance for specific applications where certain frequency responses are required. The figure provides a clear visual representation of the impact of the ratio R_1/a on the vibrational characteristics of the material, aiding in the selection and design process based on desired performance criteria.

Fig. 5 shows the relationship between the dimensionless frequency and the dimensionless Winkler coefficient for a doubly curved panel. The different curves on the graph represent different ratios of the panel's radii of curvature (R_2/R_1). The solid blue line corresponds to $R_2/R_1 = 0.5$, the dashed red line corresponds to $R_2/R_1 = 0.3$, the dashed green line corresponds to $R_2/R_1 = 0.3$, and the dashed-dotted purple line corresponds to $R_2/R_1 = 0.5$. As the dimensionless Winkler coefficient increases from 0 to 1, the dimensionless frequency also increases for all cases. This indicates that as the stiffness of the Winkler foundation increases, the natural frequencies of the panel also increase. The rate of increase and the overall value of the dimensionless frequency are influenced by the ratio of the radius of curvature. Curves with higher R_2/R_1 ratios generally show higher values of the dimensionless frequency. This suggests that the geometry of the panel, specifically the ratio of its radii of curvature, has a significant impact on its natural frequencies. Panels with a higher R_2/R_1 ratio are stiffer and thus have higher natural frequencies. In summary, the figure illustrates how the natural frequency of a doubly curved panel is affected by both the stiffness of the Winkler foundation and the geometric properties of the panel. As the stiffness of the foundation increases, the natural frequency increases. Additionally, solar cells with higher curvature ratios exhibit higher natural frequencies, emphasizing the importance of geometry in the dynamic behavior of such structures.

Fig. 6 illustrates the relationship between the dimensionless frequency and the dimensionless Winkler coefficient for a doubly curved panel. The different curves correspond to different mode shapes of the panel, denoted by the pair (m,n), where m and n represent the number of half-waves in the longitudinal and circumferential directions, respectively. The solid blue line represents the $(m,n) = (1,1)$ mode shape, the dashed red line represents the $(m,n) = (1,2)$ mode shape, the dashed green line represents the $(m,n) = (1,3)$ mode shape, and the dashed-dotted purple line represents the $(m,n) = (1,4)$ mode shape. As the dimensionless Winkler coefficient increases from 0 to 1, the dimensionless frequency also increases for all the mode shapes. The rate of increase and the overall values of ω^* vary depending on the specific mode shape. For the $(m,n) = (1,1)$ mode shape, the dimensionless frequency starts at a lower value and increases more gradually compared to the other modes. The higher the mode shape numbers m and n, the higher the initial value and the steeper the increase in ω^* as K_W^* increases. This indicates that higher mode shapes exhibit higher natural frequencies for the same value of K_W^*. The plot demonstrates that the natural frequencies of a doubly curved panel are significantly influenced by the mode shapes, with higher mode shapes resulting in higher frequencies. This relationship is crucial for understanding the dynamic behavior of such panels, particularly in applications where the panel is subject to a Winkler-type elastic foundation. The variation in frequencies with respect to the Winkler coefficient also highlights the importance of accurately modeling the elastic support in practical engineering applications, as it affects the vibrational characteristics of the structure. This information is essential for designing panels that meet specific frequency requirements and for predicting their response under different loading conditions. This analysis provides valuable insights into the vibrational behavior of doubly curved panels and underscores the need for careful consideration of both geometric parameters and foundation stiffness in their design.

Fig. 7 illustrates the relationship between the dimensionless frequency and the dimensionless Winkler coefficient for a doubly curved panel. The different curves correspond to different values of the dimensionless length scale parameter (l/h), which is related to the size effect. The solid blue line represents $l/h = 0$, the dashed red line represents $l/h = 0.5$, the dashed green line represents $l/h = 1$, and the dashed-dotted purple line represents $l/h = 1.5$. As the dimensionless Winkler coefficient increases from 0 to 1, the dimensionless frequency increases for all values of l/h. The rate of increase and the overall values of ω^* vary depending on the specific value of l/h. For $l/h = 0$, the dimensionless frequency starts at a lower value and increases gradually. As the value of l/h increases, the initial value of ω^* is higher, and the increase in ω^* with respect to K_W^* becomes more pronounced. This indicates that the size effect, represented by the length scale parameter, significantly influences the natural frequencies of the panel. Higher values of l/h result in higher natural frequencies for the same value of K_W^*. The plot demonstrates that the natural frequencies of a doubly curved panel are significantly affected by the size effect. The dimensionless length scale parameter plays a crucial role in determining the

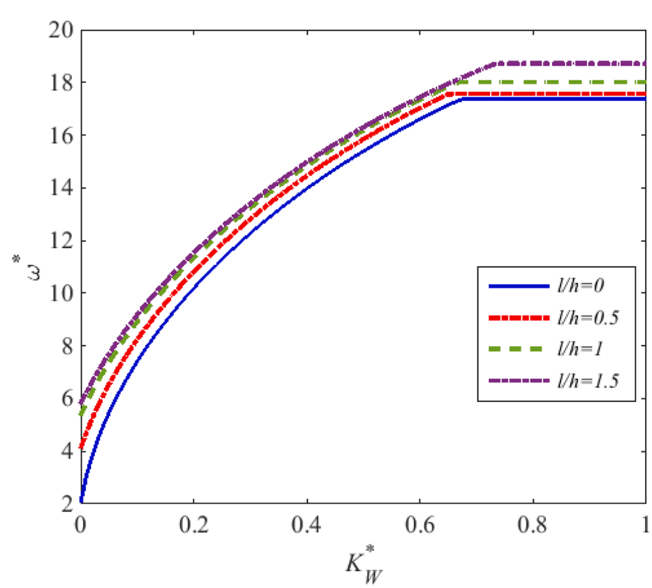

Fig. 7. Dimensionless frequency of the improved solar cell structure for various l/h values and dimensionless Winkler coefficients.

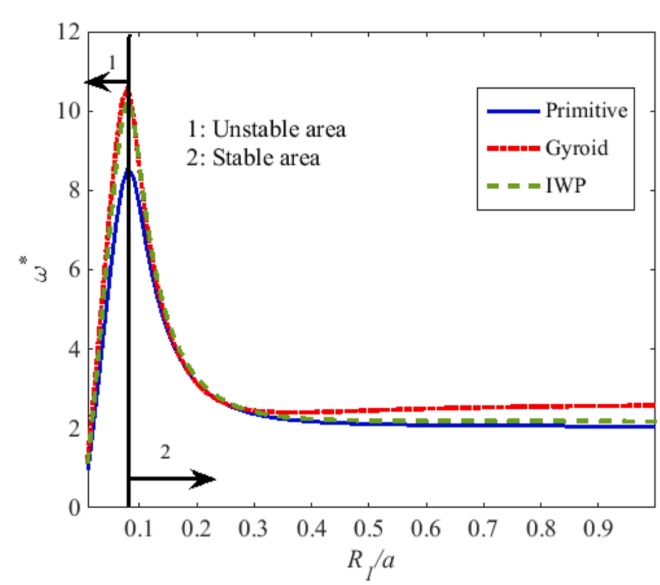

Fig. 8. Dimensionless frequency of the improved solar cell structure for various R_1/a values and TPMS architectures.

vibrational characteristics of the panel. This relationship is essential for understanding the dynamic behavior of such panels, especially in applications where the panel is supported by a Winkler-type elastic foundation. The variation in frequencies with respect to the Winkler coefficient highlights the importance of accurately modeling the elastic support and considering the size effect in practical engineering applications. This information is vital for designing panels that meet specific frequency requirements and for predicting their response under different loading conditions. The analysis provides valuable insights into the vibrational behavior of doubly curved panels and underscores the need for careful consideration of both geometric parameters and foundation stiffness in their design. The effect of the length scale parameter on the frequency response emphasizes the importance of considering size effects in the design and analysis of doubly curved panels subjected to elastic foundations.

Fig. 8 compares the dimensionless frequency of doubly curved panels with three different architectures: Primitive, Gyroid, and IWP. The x-axis represents the dimensionless R_1/a ratio, where R_1 likely indicates a characteristic length related to the panel's curvature, and a is a reference length. The y-axis shows ω^*, the dimensionless frequency. The graph is divided into two regions, marked as 1 and 2. Region 1 is identified as the "Unstable area," and region 2 as the "Stable area." At low values of R_1/a, the dimensionless frequency is significantly high, indicating instability. This behavior is consistent across all three architectures, as seen from the initial steep rise in ω^* when R_1/a is near zero. As R_1/a increases beyond approximately 0.1, the dimensionless frequency ω^* dramatically decreases and levels off. This transition marks the boundary between the unstable and stable regions. In the stable region (Region 2), ω^* values converge to around 2, indicating that the doubly curved panels with these three architectures exhibit similar stable behavior at higher R_1/a ratios. The Primitive architecture, represented by the blue solid line, shows a slightly lower peak in ω^* compared to the Gyroid and IWP architectures. The Gyroid, shown with a red dashed line, and the IWP, depicted with a green dash-dotted line, have very similar peak values and trends throughout the graph. These similarities suggest that while the different architectures influence the initial instability, their impact on stability diminishes as R_1/a increases. The convergence of the ω^* values in the stable region suggests that the geometric intricacies of the TPMS structures do not significantly affect the overall stability at higher R_1/a ratios. This stability is crucial for applications where maintaining a certain frequency response under dynamic conditions is essential. In summary, the graph illustrates the transition from instability to stability for doubly curved panels with Primitive, Gyroid, and IWP architectures, highlighting that despite initial differences in the unstable region, their stable region behavior converges.

Fig. 9 depicts the relationship between the dimensionless frequency and the ratio of the radius of curvature (R_1) to the characteristic length (a) for a doubly curved panel. Different curves represent various ratios of the panel's length scale (l) to its thickness (h). The curves are distinguished by different line styles and colors: solid blue for $l/h = 0$, dashed red for $l/h = 0.5$, dash-dotted green for $l/h = 1$, and dotted purple for $l/h = 1.5$. From the figure, we can observe that for all values of R/a, the dimensionless frequency decreases as the length scale parameter increases. This indicates that thicker panels (smaller l/h) exhibit higher dimensionless frequencies compared to thinner panels (larger l/h). As R_1/a increases from 0.1 to 0.9, all curves show a decreasing trend in ω^*, leveling off at higher values of R_1/a. For small values of R_1/a (closer to 0.1), the dimensionless frequency is high, especially for lower l/h ratios. As R_1/a increases, the frequency rapidly drops and then stabilizes around $R_1/a = 0.5$ for all l/h ratios, indicating

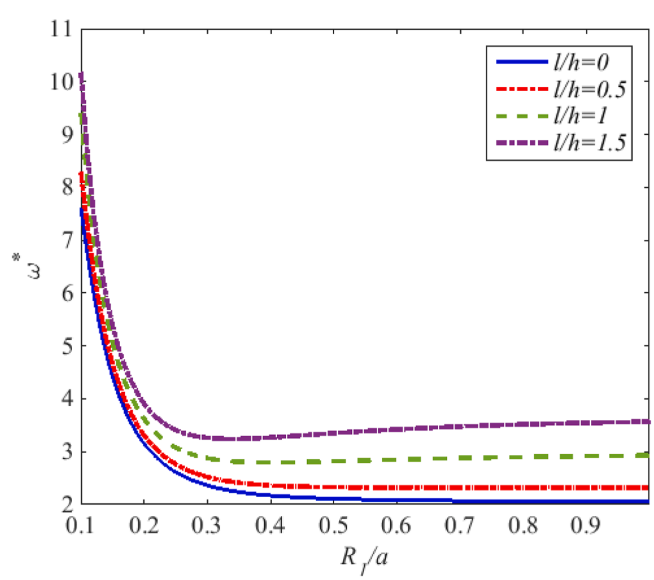

Fig. 9. Dimensionless frequency of the improved solar cell structure for various R_1/a values and l/h values.

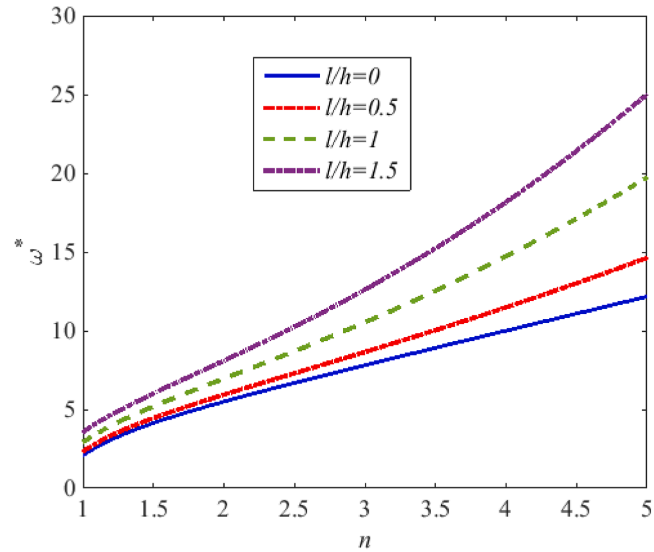

Fig. 10. Dimensionless frequency of the improved solar cell structure for various n values and l/h values.

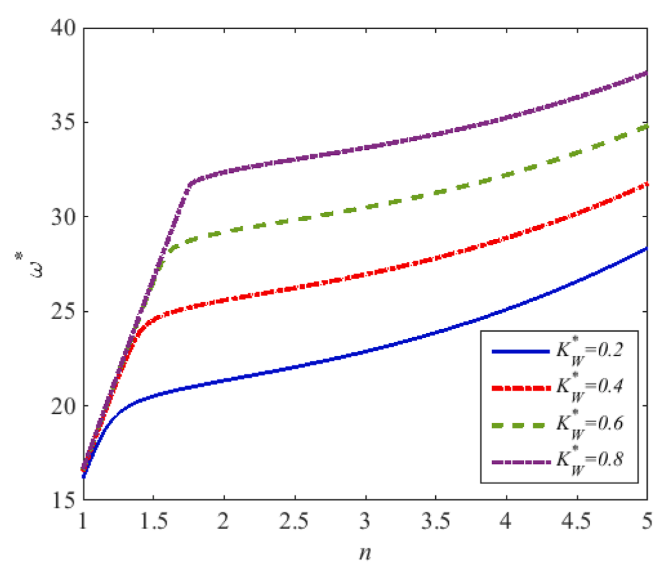

Fig. 11. Dimensionless frequency of the improved solar cell structure for various n values and K_W^* values.

a less significant change in frequency beyond this point. The stabilization implies that the curvature's influence on the dimensionless frequency becomes less pronounced as the radius of curvature increases relative to the characteristic length. In summary, the figure illustrates how the dimensionless frequency of a doubly curved panel is influenced by the curvature and thickness, with the frequency decreasing as the panel becomes thinner and as the radius of curvature increases.

Fig. 10 shows the relationship between the dimensionless frequency and the mode number (n) for a doubly curved panel. Different curves represent various length scale parameters. These ratios are denoted by different line styles and colors: solid blue for $l/h = 0$, dashed red for $l/h = 0.5$, dash-dotted green for $l/h = 1$, and dotted purple for $l/h = 1.5$. As the mode number increases from 1 to 5, the dimensionless frequency (also increases for all l/h ratios. This indicates that higher modes correspond to higher dimensionless frequencies. The rate of increase in ω^* is more pronounced for larger l/h ratios. Specifically, the curve for $l/h = 1.5$ (dotted purple) shows the steepest increase, while the curve for $l/h = 0$ (solid blue) shows the least steep increase. For each mode number, the dimensionless frequency is higher for larger l/h ratios. For example, at $n = 5$, the dimensionless frequency for $l/h = 1.5$ is around 27, whereas for $l/h = 0$, it is around 11. This suggests that as the panel becomes thinner (larger l/h ratio), the dimensionless frequency increases more rapidly with increasing mode number. In summary, the figure illustrates how the dimensionless frequency of a doubly curved panel varies with the mode number and the ratio of the panel's length to its thickness. Higher mode numbers result in higher dimensionless frequencies, and this effect is more significant for thinner panels with larger l/h ratios.

Fig. 11 illustrates the relationship between the dimensionless frequency and mode numbers for different values of K_W^*. The x-axis represents n, which could be an integer or fractional mode number or some parameter influencing the system's response. The y-axis shows ω^*, the dimensionless frequency. The different curves on the graph represent various values of K_W^*, a dimensionless stiffness parameter. The curves represent four different values of K_W^*: $K_W^* = 0.2$ (blue solid line), $K_W^* = 0.4$ (red dashed line), $K_W^* = 0.6$ (green dash-dotted line), and $K_W^* = 0.8$ (purple dash-dotted line). At $n = 1$, the dimensionless frequency starts at different values depending on K_W^*. For $K_W^* = 0.2$, ω^* starts around 16, while for $K_W^* = 0.8$, it starts around 26. As n increases, ω^* increases for all values of K_W^*, but the rate of increase and the starting values vary. For $K_W^* = 0.2$, the blue solid line shows a gradual increase in ω^* as n increases, indicating a lower stiffness resulting in lower frequencies. For $K_W^* = 0.4$, the red dashed line shows a higher initial ω^* and a steeper increase with n, indicating higher stiffness and consequently higher frequencies. The green dash-dotted line for $K_W^* = 0.6$ and the purple dash-dotted line for $K_W^* = 0.8$ follow similar trends, with even higher initial ω^* values and steeper increases as n increases. This graph demonstrates that higher K_W^* values lead to higher dimensionless frequencies for all values of n. The relationship between ω^* and n is nonlinear, with the rate of increase in ω^* becoming more pronounced for higher values of K_W^*. This indicates that the system's stiffness significantly impacts its vibrational characteristics, with stiffer systems exhibiting higher frequencies. In summary, the graph shows how the dimensionless frequency ω^* varies with the parameter n for different stiffness values K_W^*. Higher stiffness leads to higher frequencies, and the rate of increase in frequency with n is more pronounced for stiffer systems. This information is crucial for understanding the dynamic behavior of the system and designing structures with desired vibrational properties.

Fig. 12 depicts the relationship between the dimensionless frequency and the l/h ratios for three different architectures: Primitive, Gyroid, and IWP. The x-axis represents l/h, and the y-axis shows the dimensionless frequency. The curves represent three different architectures: Primitive (blue solid line), Gyroid (red dashed line), and IWP (green dash-dotted line). At lower values of l/h, all three architectures exhibit relatively lower dimensionless frequencies. As l/h increases, ω^* also increases for all three architectures, indicating a general trend of higher frequencies with increasing l/h. The Primitive architecture, represented by the blue solid line, starts with the lowest ω^* at small l/h values but shows a steady increase as l/h increases. The Gyroid architecture, depicted by the red dashed line, starts with a higher ω^* compared to the Primitive and IWP architectures at small l/h values and maintains a relatively higher frequency throughout the range of l/h. The IWP architecture, shown by the green dash-dotted line, starts with a dimensionless frequency between that of the Primitive and Gyroid architectures and follows a similar increasing trend. The differences in the curves indicate that the architecture of the material significantly influences the dimensionless frequency. The Gyroid architecture consistently exhibits the highest frequencies for given l/h values, suggesting that it might provide a stiffer or more responsive structure compared to the Primitive and IWP architectures. The Primitive architecture, while starting with the lowest frequency, shows a comparable rate of increase to the other architectures as l/h increases, eventually approaching the frequencies exhibited by the Gyroid and IWP architectures. In summary, the graph

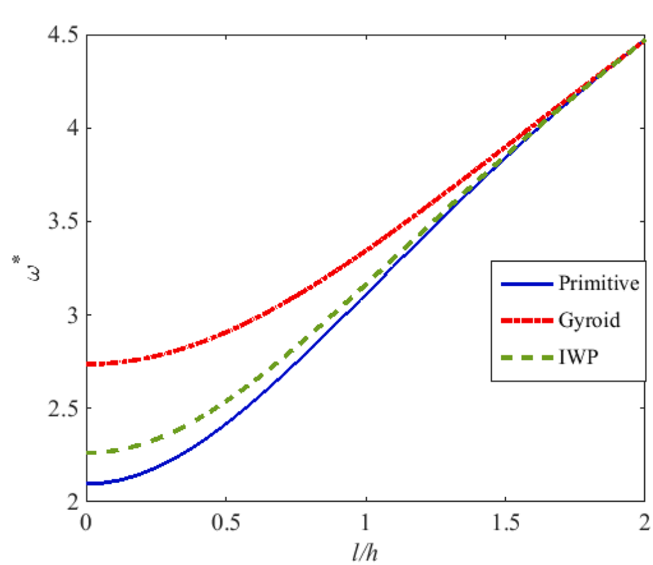

Fig. 12. Dimensionless frequency of the improved solar cell structure for various l/h values and TPMS architectures.

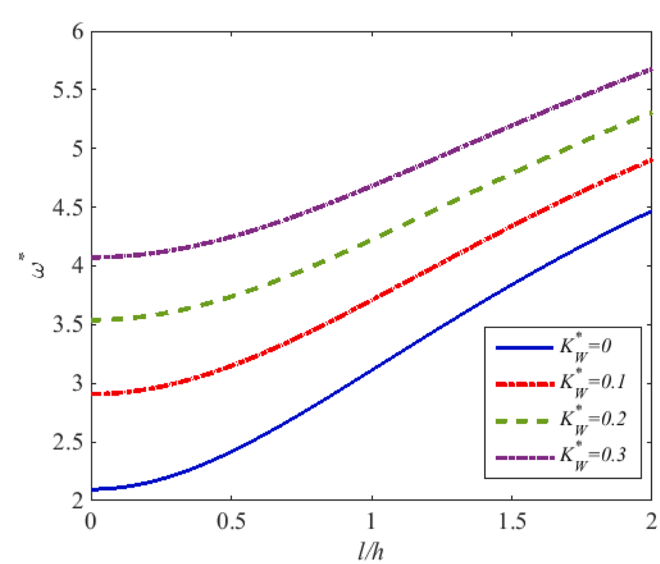

Fig. 13. Dimensionless frequency of the improved solar cell structure for various l/h, and K_W^* values.

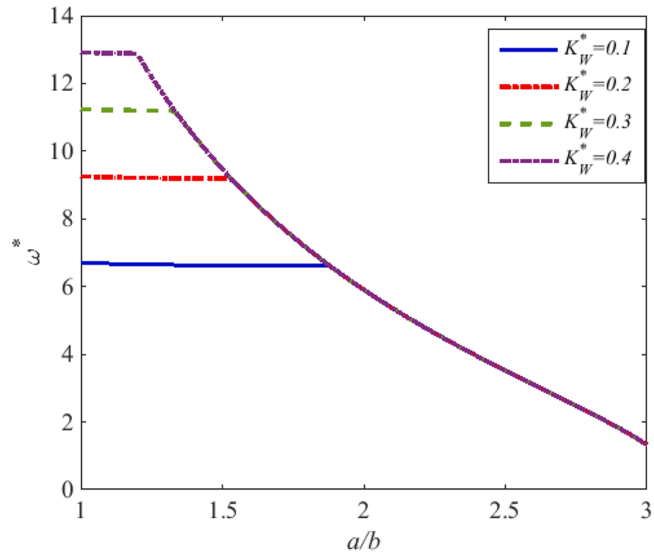

Fig. 14. Dimensionless frequency of the improved solar cell structure for various a/b, and K^*_W values.

demonstrates how the dimensionless frequency varies with the ratio l/h for three different architectures. The Gyroid architecture exhibits the highest frequencies, followed by the IWP and Primitive architectures. All three architectures show an increasing trend in frequency with increasing l/h, highlighting the influence of both the material's architecture and the geometric parameter l/h on the system's vibrational properties. This information is essential for designing materials and structures with specific dynamic characteristics.

Fig. 13 shows the relationship between the dimensionless frequency and the ratio of the length scale parameter (l) to its thickness (h) for a doubly curved panel. Different curves represent various dimensionless Winkler coefficients (K^*_W). These coefficients are distinguished by different line styles and colors: solid blue for $K^*_W = 0$, dashed red for $K^*_W = 0.1$, dash-dotted green for $K^*_W = 0.2$, and dotted purple for $K^*_W = 0.3$. As l/h increases from 0 to 2, the dimensionless frequency increases for all values of K^*_W. This trend indicates that as the panel becomes thinner (larger l/h ratio), the dimensionless frequency rises. The rate of increase in ω^* is more significant for higher values of the dimensionless Winkler coefficient. For instance, the curve for $K^*_W = 0.3$ (dotted purple) shows a steeper increase compared to the curve for $K^*_W = 0$ (solid blue). For each value of l/h, the dimensionless frequency is higher for larger K^*_W values. For example, at $l/h = 2$, the dimensionless frequency for $K^*_W = 0.3$ is around 5.5, whereas for $K^*_W = 0$, it is around 3.5. This suggests that the presence of a Winkler foundation parameter increases the stiffness of the panel, leading to higher dimensionless frequencies. In summary, the figure illustrates how the dimensionless frequency of a doubly curved panel varies with the ratio of the panel's length to its thickness and the dimensionless Winkler coefficient. As the panel becomes thinner and as the Winkler coefficient increases, the dimensionless frequency also increases, indicating a stiffer panel response to vibrational modes.

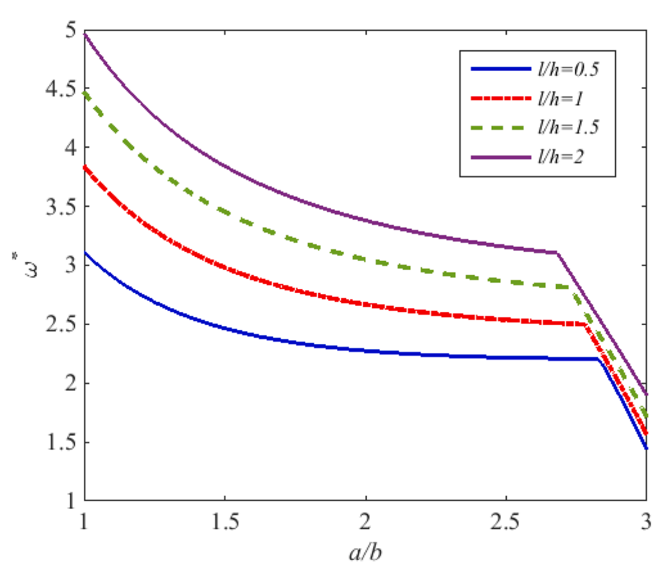

Fig. 15. Dimensionless frequency of the improved solar cell structure for various a/b, and l/h values.

Fig. 14 presents the relationship between the dimensionless frequency and the aspect ratio (a/b) for a doubly curved panel under varying dimensionless Winkler coefficients. The dimensionless frequency is plotted on the vertical axis, while the aspect ratio is shown on the horizontal axis, ranging from 1 to 3. The different curves in the plot represent different values of the dimensionless Winkler coefficient. As the aspect ratio increases from 1 to 3, the dimensionless frequency ω^* decreases for all values of K^*_W. The decrease in ω^* is more pronounced for lower values of K^*_W. For $K^*_W = 0.1$, ω^* starts around 12 and significantly drops as a/b increases, reaching around 2. For higher K^*_W values, ω^* remains relatively high and constant for lower aspect ratios before starting to decrease. The trend indicates that the influence of the Winkler coefficient on the dimensionless frequency diminishes as the aspect ratio increases. This behavior reflects how the stiffness provided by the Winkler foundation impacts the vibrational characteristics of the doubly curved panel, with higher stiffness leading to higher frequencies, particularly noticeable at lower aspect ratios.

Fig. 15 shows how the dimensionless frequency of a doubly curved panel changes with the aspect ratio for different values of l/h. On the vertical axis, the dimensionless frequency is plotted, while the aspect ratio is on the horizontal axis, ranging from 1 to 3. The various curves on the plot represent different l/h ratios. The blue solid line corresponds to $l/h = 0.5$, the red dash-dotted line to $l/h = 1$, the green dashed line to $l/h = 1.5$, and the purple dotted line to $l/h = 2$. As the aspect ratio increases, the dimensionless frequency decreases for all l/h values. This indicates that as the panel becomes longer in relation to its width, it vibrates at a lower frequency. For $l/h = 0.5$, the dimensionless frequency starts around 3 and drops to about 2 as the aspect ratio increases. For $l/h = 1$, the frequency begins just below 4 and follows a similar decreasing trend. For $l/h = 1.5$, the frequency starts around 4.5 and decreases as well. Finally, for $l/h = 2$, the frequency starts close to 5 and also decreases as the aspect ratio increases. The results show that higher l/h ratios correspond to higher dimensionless frequencies, meaning that thinner panels (relative to their length) are stiffer and vibrate at higher frequencies. However, despite the differences in l/h ratios, the dimensionless frequency consistently decreases as the aspect ratio increases. This behavior reflects the general trend that larger aspect ratios, meaning longer panels, tend to have lower natural frequencies due to their increased size relative to their thickness.

5.3. Optimized SVM-DNN-GA parameters to estimate the natural frequency of improved perovskite solar cells using datasets derived from mathematical modeling

The innovative SVM-DNN-GA algorithm is applied to estimate the natural frequency of improved perovskite solar cells using datasets derived from mathematical modeling. This approach integrates the SVM-DNN-GA algorithm to achieve accurate and efficient predictions. Here's how each component contributes to the application:

1. **Dataset Preparation**:
   - **Mathematical Modeling:** Generate a comprehensive dataset of perovskite solar cells using mathematical models. This dataset

includes various configurations, material properties, and boundary conditions, with corresponding natural frequency values.

2. **Feature Selection with SVM**:
   - **Data Preprocessing**: Use SVM to analyze the dataset and select the most influential features that impact the natural frequency. SVM helps in identifying and ranking these features based on their contribution to the prediction task.
   - **Feature Reduction**: Retain the top N features from the dataset to simplify the model and improve computational efficiency.
3. **DNN Modeling**:
   - **Network Architecture**: Design a deep neural network (DNN) with layers optimized for the selected features. The DNN model learns the complex, non-linear relationships between input features and the natural frequency.
   - **Training**: Train the DNN using the reduced dataset to capture patterns and correlations that affect the natural frequency. This training is performed using predefined hyperparameters for initial validation.
4. **Optimization with GA**:
   - **Hyperparameter Optimization**: Apply Genetic Algorithm (GA) to fine-tune the hyperparameters of the DNN, such as the number of neurons in hidden layers and the learning rate. GA iterates through various combinations to find the optimal set of hyperparameters that minimizes prediction errors.
   - **Fitness Function**: Define a fitness function that evaluates the DNN's performance based on mean squared error (MSE) of predictions. GA optimizes the DNN's architecture and training parameters to enhance predictive accuracy.
5. **Model Evaluation and Application**:
   - **Validation**: Validate the optimized DNN model using a separate portion of the dataset not seen during training. This ensures that the model generalizes well to new data.
   - **Prediction**: Use the trained and optimized DNN model to predict the natural frequency of new or modified perovskite solar cell designs. Compare predicted values with actual measurements to assess accuracy.
6. **Implementation**
   - **Design Optimization**: Utilize the predictions to inform the design and improvement of perovskite solar cells. Accurate natural frequency estimates help in optimizing the structural design to enhance performance and durability.
   - **Real-World Applications**: Apply the insights gained from the model to practical engineering problems, such as integrating the optimized solar cells into larger systems and ensuring their reliability in various operating conditions.

By leveraging this innovative machine learning approach, engineers and researchers can effectively estimate and optimize the natural frequency of perovskite solar cells, leading to improved design and performance in practical applications. In the context of estimating the natural frequency of improved perovskite solar cells using the SVM-DNN-GA algorithm, the parameters for each component are critical for optimizing performance and accuracy. Here are the typical ranges for each parameter:

1. **Support Vector Machines (SVM):**
   - **Kernel Function:** [Linear, Polynomial, RBF, Sigmoid]
   - **Kernel Coefficient (gamma):** [1e-6, 1e-5, 1e-4, 1e-3, 1e-2, 0.1, 1, 10]
   - **Regularization Parameter (C):** [0.1, 1, 10, 100, 1000]
   - **Tolerance for Stopping Criterion (tol):** [1e-4, 1e-3, 1e-2]
   - **Maximum Iterations (max_iter):** [100, 500, 1000, 5000]
2. **Deep Neural Networks (DNN):**
   - **Number of Hidden Layers:** [1, 2, 3, 4, 5]
   - **Number of Neurons per Layer:** [32, 64, 128, 256]
   - **Activation Functions:** [ReLU, Tanh, Sigmoid, Leaky ReLU]
   - **Learning Rate:** [1e-5, 1e-4, 1e-3, 1e-2, 1e-1]
   - **Batch Size:** [16, 32, 64, 128]
   - **Number of Epochs:** [50, 100, 200, 300]
   - **Optimizer:** [SGD, Adam, RMSprop]
3. **Genetic Algorithms (GA):**
   - **Population Size:** [20, 50, 100, 200]
   - **Crossover Rate:** [0.5, 0.6, 0.7, 0.8, 0.9]
   - **Mutation Rate:** [0.001, 0.01, 0.05, 0.1]
   - **Number of Generations:** [50, 100, 200, 500]
   - **Selection Method:** [Roulette wheel, Tournament, Rank-based]
   - **Crossover Method:** [Single-point, Two-point, Uniform]
   - **Mutation Method:** [Random mutation, Swap mutation, Inversion mutation]
4. **Integration Strategy:**
   - **Ensemble Method:** [Weighted averaging, Majority voting, Stacking]
   - **Weight Initialization:** [Equal weights, Random initialization within [0, 1], Based on validation performance]
   - **GA Fitness Function:** Minimize the mean squared error between predicted and actual natural frequencies
5. **Evaluation Metrics:**
   - **Mean Squared Error (MSE)**
   - **Cross-Validation Folds:** [3-fold, 5-fold, 10-fold]
   - **R-squared (R^2) Score**
   - **Training-Validation Split:** [70-30, 80-20, 90-10] split for training and validation datasets

To effectively estimate the natural frequency of improved perovskite solar cells using the SVM-DNN-GA algorithm, specific parameters for each component must be carefully selected and tuned. Here are the parameters commonly used for each component:

1. **Support Vector Machines (SVM):**
   - **Kernel Function:** Radial Basis Function (RBF) kernel
   - **Kernel Coefficient (gamma):** 0.1
   - **Regularization Parameter (C):** 1.0
   - **Tolerance for Stopping Criterion (tol):** 1e-3
   - **Maximum Iterations (max_iter):** 1000
2. **Deep Neural Networks (DNN):**
   - **Number of Hidden Layers:** 3
   - **Number of Neurons per Layer:** 128, 64, 32 (for the three layers respectively)
   - **Activation Functions:** ReLU for hidden layers, sigmoid for the output layer
   - **Learning Rate:** 0.001
   - **Batch Size:** 32
   - **Number of Epochs:** 100
   - **Optimizer:** Adam
3. **Genetic Algorithms (GA):**
   - Population Size: 50
   - **Crossover Rate:** 0.8
   - **Mutation Rate:** 0.01
   - **Number of Generations:** 100
   - **Selection Method:** Roulette wheel selection

Table 5
An analysis of the dimensionless frequency performance of the SVM-DNN-GA model at various l/h and C values

l/h	MR	Estimated		
		$C = 1$	$C = 10$	$C = 0.1$
0	11.6226	14.5926	12.7611	11.7183
0.5	16.8399	19.1466	17.2524	16.9587
1	22.4268	26.5881	24.0207	22.3641
1.5	26.2284	29.7000	27.3801	26.1723
2	33.6226	36.5926	34.7611	33.7183

Table 6
The performance of the SVM-DNN-GA model for the dimensionless frequency is assessed over a range of γ and l/h values.

l/h	MR	Estimated		
		γ =0.01	γ=0.1	γ=1
0	6.8937	9.0915	7.6956	6.9795
0.5	9.0816	11.4213	10.0353	9.1542
1	11.4081	13.7775	12.177	11.4972
1.5	14.2032	16.2789	14.9721	14.2428
2	17.8937	11.2915	16.4956	17.9795

  - **Crossover Method:** Single-point crossover
  - **Mutation Method:** Random mutation
4. **Integration Strategy:**
   - **Ensemble Method:** Weighted averaging of SVM and DNN outputs
   - **Weight Initialization:** Equal weights initially, adjusted based on validation performance
   - **GA Fitness Function:** Minimize the mean squared error between predicted and actual natural frequencies
5. **Evaluation Metrics:**
   - **Mean Squared Error (MSE)**
   - **Cross-Validation Folds:** 5-fold cross-validation
   - **R-squared (R^2) Score:** To evaluate the proportion of variance explained by the model
   - **Training-Validation Split:** 80-20 split for training and validation datasets

The method must be tuned using these parameters in order to accurately predict the natural frequency of enhanced perovskite solar cells. They support robust performance of the SVM-DNN-GA integrated strategy, improve prediction accuracy, and assist in determining the ideal model parameters. Tables 5 and 6 offer a verification using the specified parameters between the mathematical modeling and the outcomes of the trained SVM-DNN-GA algorithm. In these tables MR is mathematical modeling results.

According to Tables 5 and 6, the structure's dimensionless frequency increases as the l/h parameter increases for both the analytical and SVM-DNN-GA techniques.

So, from Tables 5 and 6 can be concluded that there is good agreement between the results of mathematical modeling and the presented hybrid algorithm via the presented parameters.

6. Conclusion

This study conclusively demonstrates the significant potential of integrating functionally graded triply periodic minimal surface layers into perovskite solar cells, specifically utilizing the primitive, gyroid, and wrapped package graph iterations. By incorporating these FG-TPMS structures into doubly curved panels and analyzing their performance through higher-order shear deformation theory and an advanced analytical method based on trigonometric functions, we have unveiled critical insights into their dynamic behavior and mechanical properties. The primitive FG-TPMS structure exhibits exceptional isotropic mechanical properties, making it a robust choice for enhancing the overall stability of solar cells. The gyroid iteration excels in optimizing stress distribution, thereby improving the durability and lifespan of the panels. The IWP design, characterized by its material efficiency, ensures that the solar cells maintain high performance with minimal material usage. Our findings indicate that the elastic substrate plays a crucial role in the overall effectiveness of the FG-TPMS layers, providing a supportive yet flexible foundation that enhances the vibrational characteristics of the panels. The trigonometric analytical method developed in this study offers precise predictions of natural frequencies and mode shapes, facilitating the fine-tuning of these structures for optimal performance. In conclusion, the integration of FG-TPMS layers represents a groundbreaking advancement in perovskite solar cell technology. In order to assess the vibrations of TPMS-reinforced perovskite solar cells surrounded by an elastic foundation, this work proposes the implementation of a novel SVM-DNN-GA algorithm employing mathematical modeling datasets. Using the SVM-DNN-GA algorithm, predicted accuracy is improved. In order to simulate and forecast the vibrational behavior of the reinforced solar cells, the integrated methodology makes use of the advantages of each technique. This innovative approach not only improves mechanical stability but also opens new avenues for future research in the application of complex geometries and functionally graded materials in photovoltaic systems. The promising results from this study lay the groundwork for further exploration and optimization of FG-TPMS structures in enhancing the next generation of solar cells.

CRediT authorship contribution statement

Qian Zhang: Investigation, Project administration, Resources, Software, Validation, Visualization, Writing – review & editing. **Qinghe Xu:** Writing – review & editing, Writing – original draft, Visualization, Validation, Supervision, Software, Resources, Investigation. **Mohammed A. El-Meligy:** Investigation, Resources, Software, Validation, Writing – review & editing. **Mehdi Tlija:** Investigation, Resources, Validation, Writing – review & editing.

Declaration of competing interest

The authors declare that they have no conflict of interest.

Data availability

Data will be made available on request.

Funding

The scientific research projects of Wenzhou University of Technology under Grant ky202304. The laboratory opening projects of Wenzhou University of Technology under Grant WLKF24007. The authors extend their appreciation to King Saud University for funding this work through Researchers Supporting Project number (RSPD2024R685), King Saud University, Riyadh, Saudi Arabia.

References

[1] M. Fu, L. Chang, H.A. Mahmoud, Enhancing the efficiency and energy capacity of the improved airplane body under external maneuvering loads, Aerosp. Sci. Technol. (2024) 109255.
[2] N.V. Nguyen, K.Q. Tran, P. Phung-Van, J. Lee, H. Nguyen-Xuan, An isogeometric analysis of functionally graded triply periodic minimal surface microplates, Aerosp. Sci. Technol. 137 (2023) 108270.
[3] N. Qiu, J. Zhang, C. Li, Y. Shen, J. Fang, Mechanical properties of three-dimensional functionally graded triply periodic minimum surface structures, Int. J. Mech. Sci. 246 (2023) 108118.
[4] C. Zhang, Z. Jiang, L. Zhao, W. Guo, Z. Jiang, X. Li, G. Chen, Mechanical characteristics and deformation mechanism of functionally graded triply periodic minimal surface structures fabricated using stereolithography, Int. J. Mech. Sci. 208 (2021) 106679.
[5] H. Nguyen-Xuan, K.Q. Tran, C.H. Thai, J. Lee, Modelling of functionally graded triply periodic minimal surface (FG-TPMS) plates, Compos. Struct. 315 (2023) 116981.
[6] X.-Y. Zhang, X.-C. Yan, G. Fang, M. Liu, Biomechanical influence of structural variation strategies on functionally graded scaffolds constructed with triply periodic minimal surface, Addit. Manuf. 32 (2020) 101015.
[7] X. Zhou, Y. Jin, J. Du, Functionally graded scaffolds with programmable pore size distribution based on triply periodic minimal surface fabricated by selective laser melting, Materials 13 (2020) 5046.
[8] H. Tang, N.V. Nguyen, H. Nguyen-Xuan, J. Lee, Isogeometric 3D optimal designs of functionally graded triply periodic minimal surface plates, Int. J. Mech. Sci. 277 (2024) 109406.

[9] S. Wang, L. Zhang, M. Tang, C. Cai, J. Wu, Z. Zhang, Y. Shi, Field-driven design and performance evaluation of dual functionally graded triply periodic minimal surface structures for additive manufacturing, Mater. Des. 233 (2023) 112257.
[10] I.M. Hassan, T.A. Enab, N. Fouda, I. Eldesouky, Design, fabrication, and evaluation of functionally graded triply periodic minimal surface structures fabricated by 3D printing, J. Braz. Soc. Mech. Sci. Eng. 45 (2023) 66.
[11] H. Guo, J. Yuan, K.K. Żu, Flutter and divergence zones of perovskite solar cell-based panels of aircraft wings in subsonic airflow, Aerosp. Sci. Technol. (2023) 108841.
[12] L. Chang, H. Wu, Y. Hu, A.M. El-Sherbeeny, Nonlinear elastic wave dispersions of solar cells strengthened by advanced functionally graded materials via both mathematical modeling and deep neural networks technique, Aerosp. Sci. Technol. 147 (2024) 109010.
[13] L. Chang, Y. Hu, A.E. Ragab, On the nonlinear wave propagations of improved solar cells, Aerosp. Sci. Technol. 146 (2024) 108941.
[14] A.S. Bati, Y.L. Zhong, P.L. Burn, M.K. Nazeeruddin, P.E. Shaw, M. Batmunkh, Next-generation applications for integrated perovskite solar cells, Commun. Mater. 4 (2023) 2.
[15] Z. Liang, Y. Zhang, H. Xu, W. Chen, B. Liu, J. Zhang, H. Zhang, Z. Wang, D.-H. Kang, J. Zeng, Homogenizing out-of-plane cation composition in perovskite solar cells, Nature 624 (2023) 557–563.
[16] S.M. Park, M. Wei, J. Xu, H.R. Atapattu, F.T. Eickemeyer, K. Darabi, L. Grater, Y. Yang, C. Liu, S. Teale, Engineering ligand reactivity enables high-temperature operation of stable perovskite solar cells, Science (1979) 381 (2023) 209–215.
[17] J. Min, S. Demchyshyn, J.R. Sempionatto, Y. Song, B. Hailegnaw, C. Xu, Y. Yang, S. Solomon, C. Putz, L.E. Lehner, An autonomous wearable biosensor powered by a perovskite solar cell, Nat. Electron. 6 (2023) 630–641.
[18] W. Peng, K. Mao, F. Cai, H. Meng, Z. Zhu, T. Li, S. Yuan, Z. Xu, X. Feng, J. Xu, Reducing nonradiative recombination in perovskite solar cells with a porous insulator contact, Science (1979) 379 (2023) 683–690.
[19] Q. Tan, Z. Li, G. Luo, X. Zhang, B. Che, G. Chen, H. Gao, D. He, G. Ma, J. Wang, Inverted perovskite solar cells using dimethylacridine-based dopants, Nature 620 (2023) 545–551.
[20] Y. Li, X. Huang, H.K. Sheriff Jr, S.R. Forrest, Semitransparent organic photovoltaics for building-integrated photovoltaic applications, Nat. Rev. Mater. 8 (2023) 186–201.
[21] C. Şirin, J. Goggins, M. Hajdukiewicz, A review on building-integrated photovoltaic/thermal systems for green buildings, Appl. Therm. Eng. 229 (2023) 120607.
[22] M. Abbasi, A.A. Nia, High-velocity impact behavior of sandwich structures with AL faces and foam cores—Experimental and numerical study, Aerosp. Sci. Technol. 105 (2020) 106039.
[23] M. Abbasi, A.A. Nia, High-velocity impact behavior of sandwich structures with AL faces and foam cores—Experimental and numerical study, Aerosp. Sci. Technol. 105 (2020) 106039.
[24] D.E. Lafi, A. Bouhadra, B. Mamen, A. Menasria, M. Bourada, A.A. Bousahla, F. Bourada, A. Tounsi, A. Tounsi, M. Yaylaci, Combined influence of variable distribution models and boundary conditions on the thermodynamic behavior of FG sandwich plates lying on various elastic foundations, Struct. Eng. Mech. 89 (2024) 103.
[25] A. Tounsi, A.A. Bousahla, S.I. Tahir, A.H. Mostefa, F. Bourada, M.A. Al-Osta, A. Tounsi, Influences of different boundary conditions and hygro-thermal environment on the free vibration responses of FGM sandwich plates resting on viscoelastic foundation, Int. J. Struct. Stab. Dyn. (2023) 2450117.
[26] A. Tounsi, A.H. Mostefa, A. Attia, A.A. Bousahla, F. Bourada, A. Tounsi, M.A. Al-Osta, Free vibration investigation of functionally graded plates with temperaturedependent properties resting on a viscoelastic foundation, Struct. Eng. Mech. Intl J. 86 (2023) 1–16.
[27] A. Tounsi, A.H. Mostefa, A.A. Bousahla, A. Tounsi, M.H. Ghazwani, F. Bourada, A. Bouhadra, Thermodynamical bending analysis of P-FG sandwich plates resting on nonlinear visco-Pasternak's elastic foundations, Steel Compos. Struct. 49 (2023) 307–323.
[28] F. Bourada, A.A. Bousahla, A. Tounsi, A. Tounsi, S.I. Tahir, M.A. Al-Osta, T. Do-Van, An integral quasi-3D computational model for the hygro-thermal wave propagation of imperfect FGM sandwich plates, Comput. Concr. 32 (2023) 61–74.
[29] I.M. Mudhaffar, A. Chikh, A. Tounsi, M.A. Al-Osta, M.M. Al-Zahrani, S.U. Al-Dulaijan, Impact of viscoelastic foundation on bending behavior of FG plate subjected to hygro-thermo-mechanical loads, Struct. Eng. Mech. Intl J. 86 (2023) 167–180.
[30] M.W. Zaitoun, A. Chikh, A. Tounsi, A. Sharif, M.A. Al-Osta, S.U. Al-Dulaijan, M. M. Al-Zahrani, An efficient computational model for vibration behavior of a functionally graded sandwich plate in a hygrothermal environment with viscoelastic foundation effects, Eng. Comput. 39 (2023) 1127–1141.
[31] M.W. Zaitoun, A. Chikh, A. Tounsi, M.A. Al-Osta, A. Sharif, S.U. Al-Dulaijan, M. M. Al-Zahrani, Influence of the visco-Pasternak foundation parameters on the buckling behavior of a sandwich functional graded ceramic–metal plate in a hygrothermal environment, Thin-Walled Struct. 170 (2022) 108549.
[32] M.A. Al-Osta, H. Saidi, A. Tounsi, S. Al-Dulaijan, M. Al-Zahrani, A. Sharif, A. Tounsi, Influence of porosity on the hygro-thermo-mechanical bending response of an AFG ceramic-metal plates using an integral plate model, Smart Struct. Syst. Int. J. 28 (2021) 499–513.
[33] T. Fu, X. Wang, T. Rabczuk, Broadband low-frequency sound insulation of stiffened sandwich PFGM doubly-curved shells with positive, negative and zero Poisson's ratio cellular cores, Aerosp. Sci. Technol. 147 (2024) 109049.
[34] Y. Bie, H. Ren, T.Q. Bui, E. Madenci, T. Rabczuk, Y. Wei, Dual-horizon peridynamics modeling of coupled chemo-mechanical-damage for interface oxidation-induced cracking in thermal barrier coatings, Comput. Methods Appl. Mech. Eng. 430 (2024) 117225.
[35] A. Ahmed, M.N. Uddin, M. Akbar, R. Salih, M.A. Khan, H. Bisheh, T. Rabczuk, Prediction of shear behavior of glass FRP bars-reinforced ultra-highperformance concrete I-shaped beams using machine learning, Int. J. Mech. Mater. Des. (2023) 1–22.
[36] I. Maskery, L. Sturm, A.O. Aremu, A. Panesar, C.B. Williams, C.J. Tuck, R. D. Wildman, I.A. Ashcroft, R.J. Hague, Insights into the mechanical properties of several triply periodic minimal surface lattice structures made by polymer additive manufacturing, Polymer. (Guildf) 152 (2018) 62–71.
[37] O. Al-Ketan, R.K. Abu Al-Rub, MSLattice: A free software for generating uniform and graded lattices based on triply periodic minimal surfaces, Mater. Des. Process. Commun. 3 (2021) e205.
[38] L. Bo, Q. Li, Y. Tian, D. Wu, Y. Yu, X. Chen, W. Gao, Nonlinear dynamic investigation of the perovskite solar cell with GPLR-FGP stiffeners under blast impact, Int. J. Mech. Sci. 213 (2022) 106866.
[39] T. Kant, K. Swaminathan, Free vibration of isotropic, orthotropic, and multilayer plates based on higher order refined theories, J. Sound Vib. 241 (2001) 319–327.
[40] J.N. Reddy, An Introduction to Nonlinear Finite Element Analysis Second Edition: with applications to heat transfer, fluid mechanics, and solid mechanics, OUP, Oxford, 2014.
[41] D.M. Sekban, E.U. Yaylacı, M.E. Özdemir, M. Yaylacı, A. Tounsi, Investigating formability behavior of friction stir-welded high-strength shipbuilding steel using experimental, finite element, and artificial neural network methods, J. Mater. Eng. Perform. (2024) 1–9.
[42] A. Garg, P. Aggarwal, Y. Aggarwal, M. Belarbi, H. Chalak, A. Tounsi, R. Gulia, Machine learning models for predicting the compressive strength of concrete containing nano silica, Comput. Concr. 30 (2022) 33.
[43] A. Garg, M.-O. Belarbi, A. Tounsi, L. Li, A. Singh, T. Mukhopadhyay, Predicting elemental stiffness matrix of FG nanoplates using Gaussian Process Regression based surrogate model in framework of layerwise model, Eng. Anal. Bound. Elem. 143 (2022) 779–795.
[44] E. Samaniego, C. Anitescu, S. Goswami, V.M. Nguyen-Thanh, H. Guo, K. Hamdia, X. Zhuang, T. Rabczuk, An energy approach to the solution of partial differential equations in computational mechanics via machine learning: Concepts, implementation and applications, Comput. Methods Appl. Mech. Eng. 362 (2020) 112790.
[45] B. Liu, W. Lu, T. Olofsson, X. Zhuang, T. Rabczuk, Stochastic interpretable machine learning based multiscale modeling in thermal conductivity of Polymeric graphene-enhanced composites, Compos. Struct. 327 (2024) 117601.
[46] C. Anitescu, E. Atroshchenko, N. Alajlan, T. Rabczuk, Artificial neural network methods for the solution of second order boundary value problems, Comput. Mater. Contin. (2019) 59.
[47] C. Anitescu, B. İsmail Ateş, T. Rabczuk, Physics-informed neural networks: Theory and applications, in: Mach. Learn. Model. Simul. Methods Appl., Springer, 2023, pp. 179–218.
[48] L. He, Y. Li, D. Torrent, X. Zhuang, T. Rabczuk, Y. Jin, Machine learning assisted intelligent design of meta structures: a review, (2023).
[49] V.M. Nguyen-Thanh, C. Anitescu, N. Alajlan, T. Rabczuk, X. Zhuang, Parametric deep energy approach for elasticity accounting for strain gradient effects, Comput. Methods Appl. Mech. Eng. 386 (2021) 114096.
[50] Y. Kiani, M. Shakeri, M. Eslami, Thermoelastic free vibration and dynamic behaviour of an FGM doubly curved panel via the analytical hybrid Laplace–Fourier transformation, Acta Mech. 223 (2012) 1199–1218.
[51] H.-S. Shen, X. Chen, L. Guo, L. Wu, X.-L. Huang, Nonlinear vibration of FGM doubly curved panels resting on elastic foundations in thermal environments, Aerosp. Sci. Technol. 47 (2015) 434–446.